

**NASA
Technical
Paper
1984**

May 1982

Planar Equations of Rollout Motion for an Aircraft With Free or Steerable Landing Gears

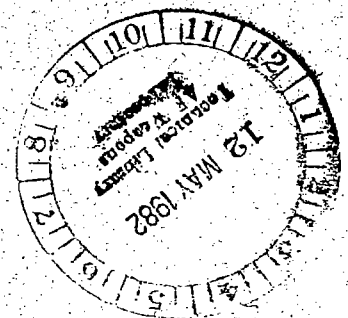
Robert K. Sleeper
and Eunice G. Smith

NASA
TP
1984
c.1



LOAN COPY: RETURN TO
AFWL TECHNICAL LIBRARY
KIRTLAND AFB, NM.

NASA





**NASA
Technical
Paper
1984**

1982

Planar Equations of Rollout Motion for an Aircraft With Free or Steerable Landing Gears

Robert K. Sleeper
and Eunice G. Smith
*Langley Research Center
Hampton, Virginia*

NASA

National Aeronautics
and Space Administration

Scientific and Technical
Information Branch

SUMMARY

Longitudinal, lateral, and heading equations of rollout motion were derived for an aircraft in a three-point attitude equipped with freely castoring or steerable landing gears and subjected to applied forces. Equilibrium constraints normal to the runway surface and about the aircraft roll and pitch axes were imposed. Transient tire forces from steady-state data were introduced by inserting a time lag between the computed tire yaw angle and the resulting tire force. The planar equations derived were used to describe the position and heading of an aircraft relative to a runway coordinate-axis system. Computed trajectories were compared with those found experimentally for a small-scale landing-gear model traversing a laterally sloping runway with and without nose-gear steering. Correlation with experiment was good. Numerical studies indicated that trajectories were sensitive to the initial translatory velocities of the test, tire drag, and angular landing-gear misalignment. The effect of the time lag on the computation of the tire forces, however, was found to be negligible for the trajectories of this paper.

INTRODUCTION

The landing of an aircraft in a strong crosswind is a difficult and possibly hazardous operation. Crosswind effects have not been as significant in the past because they have been lessened by airport design considerations such as aligning runways in the direction of prevailing winds or providing several runways with different headings. However, such considerations are not practical for all airports; and, in particular, airports envisioned for short take-off and landing (STOL) aircraft operations are expected to offer few choices of runway headings. Such runway alignment restrictions potentially expose the aircraft to higher crosswinds than those currently encountered. Furthermore, the slow landing speeds of STOL-type aircraft make them especially sensitive to crosswinds. Methods are needed to reduce this sensitivity and increase landing flexibility.

Landing-gear systems have been conceived to increase control of the aircraft on the ground in the presence of a crosswind, and tests of some crosswind gear concepts using a small model were reported in reference 1. In these tests, a laterally sloped runway provided a side component of the gravity force to simulate a crosswind. Although the model tests provided some evaluation and comparisons of the concepts, analytical techniques are needed to supplement landing-gear-system studies and provide insight into gear behavior. A set of equations of motion is required for aircraft rollout which has the capability to represent the behavior of unusual, pneumatically tired, landing-gear systems when there are sidewise external loads upon the aircraft.

Equations that describe the motion of pneumatically tired automobiles have been developed (see refs. 2 and 3), but corresponding equations that describe the aircraft rollout and taxi motion are not generally available in the literature. Reference 4 discusses the ideal track of a steered aircraft that rolls without slipping, but influences of external loads and tire behavior are missing.

This paper presents planar equations that describe the rolling motion of an aircraft in a touchdown attitude subjected to applied forces and moments and having

freely castoring or steerable landing gears equipped with pneumatic tires. Supplemental expressions are developed from tire test data relating the instantaneous forces and moments on each wheel to the wheel yaw angle. These tire-force relations can account for the tire-force buildup lagging the yaw angle, a phenomenon implied from such studies as references 5 and 6. A gravitational force appropriate to a sloped runway is included.

Computed trajectories are compared with experimental trajectories of the pneumatically tired landing-gear model of reference 1 with all gears fixed and with light nose-gear steering. The experimental trajectory data are derived from films of the tests by using the analytical photographic data-reduction method of reference 7. Effects of a number of parameters (vehicle properties and initial conditions) on the computed model trajectory with gears fixed are also investigated.

SYMBOLS

Measurements were made in U.S. Customary Units and values were converted to SI Units.

a_1, a_2	tire-moment functions, m-N and dimensionless, respectively
C_D	aerodynamic drag-force coefficient
C_L	aerodynamic lift-force coefficient
C_l	aerodynamic rolling-moment coefficient
C_m	aerodynamic pitching-moment coefficient
C_n	aerodynamic yawing-moment coefficient
C_y	aerodynamic side-force coefficient
C_1, C_2	tire side-force coefficients, N and N^{-1} , respectively
c	aerodynamic reference length, m
D	aerodynamic drag force, N
E_k	kinetic energy of vehicle, N-m
E_p	potential energy of vehicle, N-m
$F_D, F_{D,i}$	general- or ith-tire drag force directed in wheel plane (see fig. 2), N
$F_N, F_{N,i}$	general- or ith-tire force normal to runway surface (see fig. 2), N
$F_S, F_{S,i}$	general- or ith-tire side force directed normal to wheel plane (see fig. 2), N
$F_{x,A}$	component of aerodynamic force in the x-direction, N
$F_{x,T}$	component of thrust force in the x-direction, N

$F_{x,t}$ component of resultant tire forces in the x-direction, N
 F_Y aerodynamic side force (see fig. 2), N
 $F_{Y,A}$ component of aerodynamic force in the y-direction, N
 $F_{Y,T}$ component of thrust forces in the y-direction, N
 $F_{y,t}$ component of resultant tire forces in the y-direction, N
 g acceleration due to gravity, m/sec^2
 h height of vehicle center of gravity above runway surface, m
 h_D height of aerodynamic drag force above runway surface, m
 h_T height of engine thrust force above runway surface, m
 $h_{F,Y}$ height of aerodynamic side force above runway surface, m
 I_b yawing mass moment of inertia of vehicle body about the center of gravity, $kg-m^2$
 $I_{g,i}$ yawing mass moment of inertia of ith gear about its center of gravity, $kg-m^2$
 $I_{w,i}$ yawing mass moment of inertia of ith wheel about its center of gravity, $kg-m^2$
 $i = 1,2,3$ gear-identification index
 L aerodynamic lift force (see fig. 2), N
 l_t force-buildup distance of rolling tire, m
 $M_N, M_{N,i}$ general- or ith-tire moment about yaw axis (see fig. 2), N-m
 M_X aerodynamic rolling moment (see fig. 2), N-m
 M_Y aerodynamic pitching moment (see fig. 2), N-m
 M_Z aerodynamic yawing moment (see fig. 2), N-m
 $(M_Z)_{\delta,t,i}$ resultant tire yawing moment about ith gear, N-m
 $(M_Z)_{\theta,A}$ resultant aerodynamic yawing moment acting on vehicle, N-m
 $(M_Z)_{\theta,t}$ resultant tire yawing moment acting on vehicle, N-m
 m_b mass of vehicle body, kg
 $m_{g,i}$ mass of ith gear, kg

$m_{tot} = m_b + \sum_i (m_{g,i} + m_{w,i})$	mass of total vehicle, kg
$m_{w,i}$	mass of ith wheel, kg
S	aerodynamic reference area, m^2
T	engine thrust, N
t	time, sec
Δt	computational interval, sec
V_A	aerodynamic velocity (see fig. 2), m/sec
V_{cg}	velocity of vehicle center of gravity, m/sec
V_w	wind velocity (see fig. 2), m/sec
$V_{w,i}$	velocity of ith wheel, m/sec
$V_{w,n,i}$	velocity component of ith wheel normal to wheel plane, m/sec
$V_{w,p,i}$	velocity component of ith wheel in the wheel plane, m/sec
x	longitudinal runway coordinate (see fig. 1), m
x_b	longitudinal runway coordinate of vehicle-body center-of-gravity position, m
$x_{g,i}$	longitudinal runway coordinate of ith-gear center-of-gravity position, m
$x_{w,i}$	longitudinal runway coordinate of ith-wheel center-of-gravity position, m
y	lateral runway coordinate (see fig. 1), m
y_b	lateral runway coordinate of vehicle-body center-of-gravity position, m
$y_{g,i}$	lateral runway coordinate of ith-gear center-of-gravity position, m
$y_{w,i}$	lateral runway coordinate of ith-wheel center-of-gravity position, m
γ	runway slope (see fig. 2), radians, unless otherwise specified
δ, δ_i	steering angle of general or ith gear relative to the body (see fig. 1), deg
η	lateral body coordinate measured to the right of the total-vehicle center of gravity (see fig. 1), m
η_b	lateral body coordinate of vehicle-body center-of-gravity position, m
$\eta_{g,i}$	lateral body coordinate of ith-gear pivot position, m
θ	heading (crab) angle of vehicle body measured clockwise from the runway longitudinal axis (see fig. 1), radians, unless otherwise specified

λ	direction of runway slope (downhill) measured clockwise from the runway longitudinal axis (see fig. 2), deg
ξ	axial body coordinate measured forward of the total-vehicle center of gravity (see fig. 1), m
ξ_b	axial body coordinate of vehicle-body center-of-gravity position, m
$\xi_{F,Y}$	axial body coordinate of applied aerodynamic side force, m
$\xi_{g,i}$	axial body coordinate of ith-gear pivot position, m
ξ_L	axial body coordinate of applied aerodynamic lift force, m
ρ	air density, kg/m ³
$\rho_g, \rho_{g,i}$	distance of general- or ith-gear center of gravity from gear pivot (see fig. 1), m
$\rho_w, \rho_{w,i}$	distance of general- or ith-wheel center of gravity from gear pivot (see fig. 1), m
τ_i	time lag of ith-rolling-tire-force buildup, sec
ϕ	direction angle of vehicle velocity measured clockwise from runway longitudinal axis (see fig. 2), radians
ϕ_w	direction angle of wind velocity measured clockwise from runway longitudinal axis (see fig. 2), radians
ψ, ψ_i	general- or ith-tire yaw angle, radians, unless otherwise specified
ψ_e	effective (delayed) tire yaw angle, radians, unless otherwise specified

The operator ∂ denoted partial differentiation, $\frac{d}{dt}$ or a dot over a variable denotes differentiation with respect to time, and $\text{sgn}(\)$ denotes the sign of the argument in the parenthesis.

IDEALIZED VEHICLE

A schematic representation of a rolling aircraft with steerable landing gears in a three-point landing attitude is depicted in figure 1. A system of four interconnected rigid bodies represents the main body of the aircraft and three landing gears. Planar motion is assumed for the body with longitudinal, lateral, and heading degrees of freedom, and a swiveling degree of freedom is included for each gear. Equilibrium conditions normal to the plane of the runway and about the aircraft pitch and roll axes are assumed.

Space-fixed x,y -coordinate axes are defined with the x -axis directed down range and the y -axis directed to the right. Body-fixed ξ,η -coordinate axes are defined with the origin at the center of gravity (c.g.) of the complete aircraft with undeflected gears. The x,y -coordinates describe the motion of the ξ,η -origin. The angle θ between the x - and ξ -axes denotes aircraft heading, and the angles δ_i ($i = 1,2,3$) denote deflected angles of the swiveling gears relative to the body. The

symbols $\rho_{g,i}$ and $\rho_{w,i}$ denote distances from the gear pivot point to the c.g. of the gear (less the wheel) and to the c.g. of the wheel, respectively.

The forces and moments applied to the vehicle are indicated in figure 2. Included are aerodynamic forces and moments, an engine thrust force, tire forces, and a gravity force due to runway slope. The effect of runway slope, which is shown as a true angle in the edge view of the runway, is not generally a consideration but has been included in this report to correlate with the tests of reference 1.

EQUATIONS OF MOTION

The method of Lagrange (see refs. 8 and 9, for instance) is used to develop the equations of motion of the vehicle. Except for the gravity forces attributed to the sloped runway which are derived from the potential energy, the forces and moments acting on the vehicle are directly specified. The forms of the generating equations in terms of the longitudinal, lateral, heading, and swiveling-gear degrees of freedom, respectively, are given by

$$\frac{d}{dt} \left(\frac{\partial E_k}{\partial \dot{x}} \right) - \frac{\partial E_k}{\partial x} + \frac{\partial E_p}{\partial x} = F_{x,T} + F_{x,A} + F_{x,t} \quad (1)$$

$$\frac{d}{dt} \left(\frac{\partial E_k}{\partial \dot{y}} \right) - \frac{\partial E_k}{\partial y} + \frac{\partial E_p}{\partial y} = F_{y,T} + F_{y,A} + F_{y,t} \quad (2)$$

$$\frac{d}{dt} \left(\frac{\partial E_k}{\partial \dot{\theta}} \right) - \frac{\partial E_k}{\partial \theta} + \frac{\partial E_p}{\partial \theta} = (M_z)_{\theta,A} + (M_z)_{\theta,t} \quad (3)$$

$$\frac{d}{dt} \left(\frac{\partial E_k}{\partial \dot{\delta}_i} \right) - \frac{\partial E_k}{\partial \delta_i} + \frac{\partial E_p}{\partial \delta_i} = (M_z)_{\delta,t,i} \quad (\text{For } i = 1, 2, 3) \quad (4)$$

where E_k and E_p are the kinetic- and potential-energy functions of the system of rigid bodies, respectively, and the nongravitational vehicle forces and moments are indicated by the terms on the right-hand side of the equations.

Kinetic-Energy Function

The kinetic energy, the sum of energy from motions of the body and the gears, is expressed by

$$E_k = \frac{1}{2} \left[m_b (\dot{x}_b^2 + \dot{y}_b^2) + I_b \dot{\theta}^2 \right] + \frac{1}{2} \sum_i \left[m_{g,i} (\dot{x}_{g,i}^2 + \dot{y}_{g,i}^2) + m_{w,i} (\dot{x}_{w,i}^2 + \dot{y}_{w,i}^2) + (I_{g,i} + I_{w,i}) (\dot{\delta}_i + \dot{\theta})^2 \right] \quad (5)$$

where

$$\dot{x}_b = \dot{x} - \dot{\theta} (\xi_b \sin \theta + \eta_b \cos \theta) \quad (6)$$

$$\dot{y}_b = \dot{y} + \dot{\theta}(\xi_b \cos \theta - \eta_b \sin \theta) \quad (7)$$

$$\dot{x}_{g,i} = \dot{x} - \dot{\theta}(\xi_{g,i} \sin \theta + \eta_{g,i} \cos \theta) + \rho_{g,i}(\dot{\theta} + \dot{\delta}_i) \sin(\theta + \delta_i) \quad (8)$$

$$\dot{y}_{g,i} = \dot{y} + \dot{\theta}(\xi_{g,i} \cos \theta - \eta_{g,i} \sin \theta) - \rho_{g,i}(\dot{\theta} + \dot{\delta}_i) \cos(\theta + \delta_i) \quad (9)$$

$$\dot{x}_{w,i} = \dot{x} - \dot{\theta}(\xi_{g,i} \sin \theta + \eta_{g,i} \cos \theta) + \rho_{w,i}(\dot{\theta} + \dot{\delta}_i) \sin(\theta + \delta_i) \quad (10)$$

$$\dot{y}_{w,i} = \dot{y} + \dot{\theta}(\xi_{g,i} \cos \theta - \eta_{g,i} \sin \theta) - \rho_{w,i}(\dot{\theta} + \dot{\delta}_i) \cos(\theta + \delta_i) \quad (11)$$

Potential-Energy Function

The gravity forces, derived from the potential-energy function of the vehicle components, are given as follows:

$$\begin{aligned} E_p = & -g\gamma [m_b [x \cos \lambda + y \sin \lambda + \xi_b \cos(\lambda - \theta) + \eta_b \sin(\lambda - \theta)] \\ & + \sum_i \{(m_{g,i} + m_{w,i}) [x \cos \lambda + y \sin \lambda \\ & + \xi_{g,i} \cos(\lambda - \theta) + \eta_{g,i} \sin(\lambda - \theta)]\} \\ & - \sum_i [(m_{g,i} \rho_{g,i} + m_{w,i} \rho_{w,i}) \cos(\lambda - \theta - \delta_i)] \end{aligned} \quad (12)$$

where g is the acceleration due to gravity, γ is the runway slope (assumed to be small), and λ is the direction of the downhill slope.

Equations of Motion

The equations of motion are found by performing the indicated mathematical operations specified in equations (1) to (4). After reducing and rearranging terms, the following six equations of motion are obtained:

Longitudinal motion:

$$\begin{aligned}
\ddot{x}_{m_{\text{tot}}} - \ddot{\theta} \{m_b (\xi_b \sin \theta + \eta_b \cos \theta) + \sum_i [(m_{g,i} + m_{w,i}) (\xi_{g,i} \sin \theta + \eta_{g,i} \cos \theta)] \\
- \sum_i [(m_{g,i} \rho_{g,i} + m_{w,i} \rho_{w,i}) \sin (\theta + \delta_i)]\} \\
+ \sum_i [\ddot{\delta}_i (m_{g,i} \rho_{g,i} + m_{w,i} \rho_{w,i}) \sin (\theta + \delta_i)] \\
- \dot{\theta}^2 \{m_b (\xi_b \cos \theta - \eta_b \sin \theta) + \sum_i [(m_{g,i} + m_{w,i}) (\xi_{g,i} \cos \theta - \eta_{g,i} \sin \theta)]\} \\
+ \sum_i [(\dot{\theta} + \dot{\delta}_i)^2 (m_{g,i} \rho_{g,i} + m_{w,i} \rho_{w,i}) \cos (\theta + \delta_i)] - g \gamma m_{\text{tot}} \cos \lambda \\
= F_{x,T} + F_{x,A} + F_{x,t}
\end{aligned} \tag{13}$$

Lateral motion:

$$\begin{aligned}
\ddot{y}_{m_{\text{tot}}} + \ddot{\theta} \{m_b (\xi_b \cos \theta - \eta_b \sin \theta) + \sum_i [(m_{g,i} + m_{w,i}) (\xi_{g,i} \cos \theta - \eta_{g,i} \sin \theta)] \\
- \sum_i [(m_{g,i} \rho_{g,i} + m_{w,i} \rho_{w,i}) \cos (\theta + \delta_i)]\} \\
- \sum_i [\ddot{\delta}_i (m_{g,i} \rho_{g,i} + m_{w,i} \rho_{w,i}) \cos (\theta + \delta_i)] \\
- \dot{\theta}^2 \{m_b (\xi_b \sin \theta + \eta_b \cos \theta) + \sum_i [(m_{g,i} + m_{w,i}) (\xi_{g,i} \sin \theta + \eta_{g,i} \cos \theta)]\} \\
+ \sum_i [(\dot{\theta} + \dot{\delta}_i)^2 (m_{g,i} \rho_{g,i} + m_{w,i} \rho_{w,i}) \sin (\theta + \delta_i)] - g \gamma m_{\text{tot}} \sin \lambda \\
= F_{y,T} + F_{y,A} + F_{y,t}
\end{aligned} \tag{14}$$

Heading motion:

$$\begin{aligned}
& -\ddot{x} \{ m_b (\xi_b \sin \theta + \eta_b \cos \theta) + \sum_i [(m_{g,i} + m_{w,i}) (\xi_{g,i} \sin \theta + \eta_{g,i} \cos \theta)] \\
& \quad - \sum_i [(m_{g,i} \rho_{g,i} + m_{w,i} \rho_{w,i}) \sin (\theta + \delta_i)] \} \\
& + \ddot{y} \{ m_b (\xi_b \cos \theta - \eta_b \sin \theta) + \sum_i [(m_{g,i} + m_{w,i}) (\xi_{g,i} \cos \theta - \eta_{g,i} \sin \theta)] \\
& \quad - \sum_i [(m_{g,i} \rho_{g,i} + m_{w,i} \rho_{w,i}) \cos (\theta + \delta_i)] \} \\
& + \ddot{\theta} \{ I_b + m_b (\xi_b^2 + \eta_b^2) + \sum_i [I_{g,i} + I_{w,i} + (m_{g,i} + m_{w,i}) (\xi_{g,i}^2 + \eta_{g,i}^2) \\
& \quad + m_{g,i} \rho_{g,i}^2 + m_{w,i} \rho_{w,i}^2 \\
& \quad - 2(m_{g,i} \rho_{g,i} + m_{w,i} \rho_{w,i}) (\xi_{g,i} \cos \delta_i + \eta_{g,i} \sin \delta_i)] \} \\
& + \sum_i \{ \ddot{\delta}_i [I_{g,i} + I_{w,i} + (m_{g,i} \rho_{g,i}^2 + m_{w,i} \rho_{w,i}^2) \\
& \quad - (m_{g,i} \rho_{g,i} + m_{w,i} \rho_{w,i}) (\xi_{g,i} \cos \delta_i + \eta_{g,i} \sin \delta_i)] \} \\
& + \sum_i [(2\theta \dot{\delta}_i + \dot{\delta}_i^2) (m_{g,i} \rho_{g,i} + m_{w,i} \rho_{w,i}) (\xi_{g,i} \sin \delta_i - \eta_{g,i} \cos \delta_i)] \\
& - g \gamma \{ m_b [\xi_b \sin (\lambda - \theta) - \eta_b \cos (\lambda - \theta)] \\
& + \sum_i (m_{g,i} + m_{w,i}) [\xi_{g,i} \sin (\lambda - \theta) - \eta_{g,i} \cos (\lambda - \theta)] \\
& - \sum_i [(m_{g,i} \rho_{g,i} + m_{w,i} \rho_{w,i}) \sin (\lambda - \theta - \delta_i)] \} \\
& = (M_z)_{\theta, A} + (M_z)_{\theta, t}
\end{aligned} \tag{15}$$

Gear motion for each gear where $i = 1, 2,$ and 3 :

$$\begin{aligned}
 & \ddot{x}(m_{g,i}\rho_{g,i} + m_{w,i}\rho_{w,i}) \sin(\theta + \delta_i) - \ddot{y}(m_{g,i}\rho_{g,i} + m_{w,i}\rho_{w,i}) \cos(\theta + \delta_i) \\
 & + \ddot{\theta} [I_{g,i} + I_{w,i} + m_{g,i}\rho_{g,i}^2 + m_{w,i}\rho_{w,i}^2 \\
 & - (m_{g,i}\rho_{g,i} + m_{w,i}\rho_{w,i})(\xi_{g,i} \cos \delta_i + \eta_{g,i} \sin \delta_i)] \\
 & + \ddot{\delta}_i (I_{g,i} + I_{w,i} + m_{g,i}\rho_{g,i}^2 + m_{w,i}\rho_{w,i}^2) \\
 & - \dot{\theta}^2 (m_{g,i}\rho_{g,i} + m_{w,i}\rho_{w,i})(\xi_{g,i} \sin \delta_i - \eta_{g,i} \cos \delta_i) \\
 & + g\gamma(m_{g,i}\rho_{g,i} + m_{w,i}\rho_{w,i}) \sin(\lambda - \theta - \delta_i) \\
 & = (M_z)_{\delta,t,i} \tag{16}
 \end{aligned}$$

FORCES AND MOMENTS ON VEHICLE

Expressions for the forces and moments appearing in the equations of motion are developed in the following sections and include effects of engine thrust, aerodynamics, and tire behavior.

Engine Thrust

An engine-thrust force T is assumed to be aligned with the vehicle center line and gives x, y components

$$F_{x,T} = T \cos \theta \tag{17}$$

$$F_{y,T} = T \sin \theta \tag{18}$$

Aerodynamic Forces and Moments

Simple aerodynamic relationships including the effects of wind are

$$L = \frac{1}{2} \rho V_A^2 S C_L \tag{19}$$

$$D = \frac{1}{2} \rho V_A^2 S C_D \tag{20}$$

$$F_Y = \frac{1}{2} \rho V_A^2 S C_Y \tag{21}$$

$$M_Y = \frac{1}{2} \rho V_A^2 S c C_m \quad (22)$$

$$M_Z = \frac{1}{2} \rho V_A^2 S c C_n \quad (23)$$

$$M_X = \frac{1}{2} \rho V_A^2 S c C_l \quad (24)$$

where ρ is the atmospheric density and V_A is an aerodynamic velocity defined as the vector sum of the vehicle and wind velocities as shown in figure 2. The factor V_A^2 is computed by

$$V_A^2 = V_{cg}^2 + V_w^2 + 2V_{cg} V_w \cos(\phi_w - \phi) \quad (25)$$

$$V_{cg} = (x^2 + y^2)^{1/2} \quad (26)$$

$$\phi = \tan^{-1} \frac{\dot{y}}{\dot{x}} \quad (27)$$

where V_w and ϕ_w denote the magnitude and direction of headwind, respectively.

The aerodynamic drag force D , side force F_Y , and yawing moment M_Z combine into the following forces and moments appearing, respectively, in the longitudinal, lateral, and heading equations:

$$F_{X,A} = -D \cos \theta - F_Y \sin \theta \quad (28)$$

$$F_{Y,A} = -D \sin \theta + F_Y \cos \theta \quad (29)$$

$$\left(M_Z \right)_{\theta,A} = M_Z + \xi_{F,Y} F_Y \quad (30)$$

where $\xi_{F,Y}$ is the axial position of the side force applied to the vehicle in the body coordinate system.

Tire Forces and Moments

The tire forces for each gear i are described in terms of a drag force $F_{D,i}$ in the plane of the wheel, a side force $F_{S,i}$ normal to the plane, and a moment $M_{N,i}$ about an axis normal to the runway surface and through the wheel center as shown in figure 2. When the components of the tire forces are resolved, the following relations are obtained:

$$F_{x,t} = - \sum_i [F_{D,i} \cos (\theta + \delta_i) + F_{S,i} \sin (\theta + \delta_i)] \quad (31)$$

$$F_{y,t} = - \sum_i [F_{D,i} \sin (\theta + \delta_i) - F_{S,i} \cos (\theta + \delta_i)] \quad (32)$$

$$\begin{aligned} (M_z)_{\theta,t} = & - \sum_i [F_{D,i} (\xi_{g,i} \sin \delta_i - \eta_{g,i} \cos \delta_i) \\ & - F_{S,i} (\xi_{g,i} \cos \delta_i + \eta_{g,i} \sin \delta_i - \rho_{w,i}) - M_{N,i}] \end{aligned} \quad (33)$$

$$(M_z)_{\delta,t,i} = -F_{S,i} \rho_{w,i} + M_{N,i} \quad (34)$$

The individual tire forces and moments $F_{D,i}$, $F_{S,i}$, and $M_{N,i}$ appearing on the right side of equations (31) to (34) may be functions of tire yaw angle, normal force, and forward velocity, respectively.

Yaw-angle formulation.— The tire yaw angle, that is, the clockwise angle that the translational velocity vector of the tire makes with the wheel plane, may be defined by using local instantaneous velocity components of the tire as

$$\phi_i = \tan^{-1} \frac{V_{w,n,i}}{V_{w,p,i}} \quad (35)$$

where $V_{w,n,i}$, the velocity component normal to the wheel plane, is given as

$$\begin{aligned} V_{w,n,i} = & V_{cg} \sin (\phi - \theta - \delta_i) \\ & + \dot{\theta} (\xi_{g,i} \cos \delta_i + \eta_{g,i} \sin \delta_i - \rho_{w,i}) - \rho_{w,i} \dot{\delta}_i \end{aligned} \quad (36)$$

and $V_{w,p,i}$, the velocity component parallel to the wheel plane, is given as

$$V_{w,p,i} = V_{cg} \cos (\phi - \theta - \delta_i) + \dot{\theta} (\xi_{g,i} \sin \delta_i - \eta_{g,i} \cos \delta_i) \quad (37)$$

The buildup of rolling-tire forces lags the imposed yaw angle in time. Such a delay is implied from the tests of reference 5 which show the distance that an initially yawed tire must roll before the full side force is developed, and the lag can also be implied from the hysteretic tire-force—yaw-angle relationships found in reference 6 for tires tested on a dynamometer. A delay may be introduced by defining an effective yaw angle $\psi_{e,i}$ related to the instantaneous yaw angle ϕ_i by the relationship

$$\psi_{e,i} + \tau_i \dot{\psi}_{e,i} = \phi_i \quad (38)$$

where τ_i is the duration of the time lag. The time lag may be expressed by the formula

$$\tau_i = \frac{l_t}{V_{w,i}} \quad (39)$$

where l_t is the distance that a tire must roll for a force to be developed and

$V_{w,i}$ is the wheel velocity $\sqrt{V_{w,p,i}^2 + V_{w,n,i}^2}$. For such an assumption, equation (38) becomes

$$\psi_{e,i} + \frac{l_t}{V_{w,i}} \dot{\psi}_{e,i} = \psi_i \quad (40)$$

For a computer program, a finite-difference form of equation (40) is utilized and is given by

$$\psi_{e,i}(t) = \frac{\psi_i(t) + \left(\frac{l_t}{V_{w,i}(t) \Delta t} \right) \psi_{e,i}(t - \Delta t)}{1 + \frac{l_t}{V_{w,i}(t) \Delta t}} \quad (41)$$

where Δt is the time step and the derivative of the effective yaw angle is approximated by

$$\dot{\psi}_{e,i}(t) = \frac{\psi_{e,i}(t) - \psi_{e,i}(t - \Delta t)}{\Delta t} \quad (42)$$

Equilibrium equations.— When force equilibrium normal to the runway surface and moment equilibrium about the pitch and roll axes of the vehicle are imposed, the gear normal forces may be related as follows:

Aircraft normal-force equation:

$$\sum_i F_{N,i} = m_{tot} g \cos \gamma - L \quad (43)$$

Aircraft pitch-axis equation:

$$\sum_i F_{N,i} (\xi_{g,i} - \rho_{w,i} \cos \delta_i) = h \sum_i (F_{D,i} \cos \delta_i + F_{S,i} \sin \delta_i) - M_Y - L \xi_L - D(h_D - h) + T(h_T - h) \quad (44)$$

Aircraft roll-axis equation:

$$\sum_i F_{N,i} (\eta_{g,i} - \rho_{w,i} \sin \delta_i) = h \sum_i (F_{D,i} \sin \delta_i - F_{S,i} \cos \delta_i) + M_X + F_Y (h_{F,Y} - h) \quad (45)$$

TRAJECTORY-COMPUTATION PROCEDURE

The equations of vehicle motion have been programmed for numerical solution on a high-speed digital computer. The method for computing a trajectory follows.

Aerodynamic forces are computed first by using equations (19) to (27). Also, except at touchdown when the effective yaw angle $\psi_{e,i}$ is assumed to be zero, the tire yaw angles are computed from equations (35) to (37) and (41). Tire forces are then solved iteratively beginning with an estimate of the normal gear forces. Tire drag and side forces are computed and revised normal forces are solved from the equilibrium equations (43) to (45). The original and revised normal forces are averaged and the normal-force solution is repeated until all of the tire normal forces for two consecutive iterations agree within a specified tolerance. Following convergence, the normal-force values are used to compute tire moments which (together with the tire, aerodynamic, and thrust forces) are introduced into equations (17), (18), and (28) to (34) for substitution into equations (13) to (16). Individual accelerations for each degree of freedom are obtained from a simultaneous solution of the equations of motion. The accelerations are numerically integrated twice to yield new trajectory variables. The new variables and their derivatives replace the original variables, and the computational sequence is repeated for subsequent time intervals.

When gear angles δ_i are specified, appropriate time histories of the angles and their derivatives must be supplied in place of the gear equations (16). Closed-loop steering control also can be implemented with minor modifications, but this consideration is beyond the scope of this study.

APPLICATIONS AND DISCUSSION

The equations of motion were applied to predict the rolling-trajectory trends of the tests conducted in the study of reference 1. The equations were also used to determine the relative sensitivity of the trajectory to several parameters.

Model Tests

Description of model and test conditions.- A photograph of the instrumented model used in reference 1 is shown in figure 3. The model has a triangularly shaped body with three gears which can be locked, steered, or swiveled freely. Targets were installed to facilitate trajectory measurements using optical techniques.

The model tests were conducted in the enclosed facility shown in figure 4. The photograph shows the 4.1-m-wide runway, the launching apparatus, and the test model (prior to instrumentation). The runway was tilted 4.5° to the left, i.e., the left edge of the runway was lower than the right. Basic properties of the model are given in table I. Although the model was not completely scaled to a specific aircraft, it was representative of a one-seventh-scale model of a STOL-type aircraft.

Tire properties.- Tire force and moment relationships required for the pneumatic-model airplane tires of this study are derived from dynamometer tests. Measurements were made by using one tire and landing gear of reference 1, and the results are discussed in the appendix where tire forces and moments are expressed as functions of tire yaw angle and vertical loading under steady-state conditions. The tests showed that forward velocity had little influence on the measured forces.

(Ref. 2, in citing the work of L. Huber, confirmed that the tire side force is practically independent of velocity.)

The functional relationships adopted for force and moment relationships for each tire are given as follows in terms of the tire yaw angle ψ and normal force F_N :

$$F_D = F_D(\psi, F_N) \quad (46)$$

$$F_S = -C_1 \left(1 - e^{-C_2 F_N} \right) \psi \quad (47)$$

$$M_N = -a_1(F_N) \left[1 - e^{-a_2(F_N) |\psi|} \right] \text{sgn}(\psi) \quad (48)$$

Trajectory measurement.- The trajectory of the model was obliquely photographed from above the runway by 16-mm motion-picture cameras. One camera was positioned slightly behind the touchdown point, its view extending from the touchdown point to 7.5 m beyond it; and another camera was positioned to view the region 6.5 to 15 m beyond the touchdown point. The position and heading of the model were determined from the motion-picture records of a test using the method of reference 7.

Numerical Results

The equations of motion are applied to two tests using the model and test conditions of reference 1. One, an unreported test, had the gears of the model fixed; and the other, case 5 of reference 1, had light steering of the nose gear. Only forces due to gravity and to the tires were considered. The downhill slope to the left was specified by a slope γ of 4.5° and by a slope direction λ of -90° .

Steady-state tire-force relationships for an unbraked 11.4-cm-diameter pneumatic model of an aircraft tire, used in the model tests, are presented in the appendix. Approximate drag-force data measured in the tests are also given in the appendix. The values vary erratically, suggesting random errors as large as the measured quantities. However, the drag-force variations were treated herein as representative of the model gears, and for this study, the drag force for each gear was simply linearly interpolated with respect to both normal force F_N and yaw angle ψ . The tire-side-force expression is given by equation (A1) of the appendix for which, in the computations, the coefficients C_1 and C_2 of equation (47) are 5.01 N and 0.0422 N^{-1} , respectively, where the angular units are in degrees. Similarly, the tire-moment data of the appendix are given by equation (48) for which the functions $a_1(F_N)$ and $a_2(F_N)$ are interpolated from the logarithmic form of the functions displayed in the appendix by using a cubic-spline curve-fitting procedure.

The experimental force-motion relationship includes effects due to both a simple tire slip and a coupled rolling- and lateral-deformation interaction. However, the tire representation of the computer program includes no mechanism to account for the deformation interaction.

Both tire side force and moment were assumed to be zero at touchdown; and for the effective yaw-angle computations, the force-buildup distance of the rolling tire l_t was assumed to be constant. The buildup distance was determined from a test for which the yaw angle was varied in time. For this test, at a surface speed of 4.6 m/sec , the tire-side-force development was found to lag the input yaw angle by

0.021 sec. A distance Δt of 9.6 cm was computed from the lag by using equation (39). The steering input was specified directly from the gear-position time histories of the steered test of reference 1; the steering angle was piecewise linearly interpolated between discrete values of the data, and derivatives were derived from a parabolic least-squares polynomial approximation to five running data points. The model mass and configuration properties of table I were used to describe the vehicle.

Correlation of unsteered run.- For the unsteered run, the gears were fixed in the undeflected position and the model was launched along the x-axis of the laterally sloped runway at a speed of 4.41 m/sec. The test duration was limited to 2.4 sec, which was the time that the model remained on the runway.

Figure 5 shows measured positions and headings and faired time histories of the data. The right side of the figure displays position and heading at 0.25-sec time increments where the arrows denote the simulated wind direction. The optical-trajectory-measurement technique indicates the model response, producing consistent results with little scatter for the position measurements. The scatter, present in the heading measurements during the early part of the trajectory, is attributed to the optical and possibly to the mechanical performance of the first camera and (unsymmetric) model bouncing actions.

The measured trajectory data show that the model initially drifts slightly laterally downhill before quickly heading uphill. For the duration of the test, the longitudinal-distance time history is essentially linear, implying small retarding forces and, hence, nearly constant speed.

When the forward velocity of touchdown of $\dot{x}(0) = 4.41$ m/sec and all other initial conditions equal to zero were input into the analytic procedure, the trajectory shown in figure 6 was obtained. The faired experimental trajectory data of figure 5, denoted by the dashed line, are also included.

The lateral-distance and heading-angle time histories of figure 6 show the characteristic, brief, lateral, downwind excursion and the subsequent upwind drift. Similar behavior has been observed in studies of the lateral response of rolling automobiles to side loads. For instance, reference 10 indicates such an automobile response and indicates that vehicles with pneumatic tires such as those on the model may drift laterally with or without changing heading. A heading change occurs when the yawing moment is unbalanced; that is, the applied forces and their reaction produce a moment about the vehicle c.g. Since the model yaws upwind, the resultant lateral tire force must be forward of the c.g. Such a forward tire force for the weight distribution is attributed to the saturation nature of the tire side-force relationship with normal load shown in the appendix. If the side-force relationship were linear, for instance, computed results show that the model rolls without lateral or heading excursions. For the conditions of figure 6, the lateral response is shown to be primarily dependent upon the heading behavior. The slight initial lateral drift occurs until the unbalance in forces and moments on the gears results in an upwind drift of the vehicle.

The results indicate that the system of equations, including the assumed equilibrium and tire-force relations, is adequate to provide rollout trajectory trends of aircraft with pneumatic tires. The slight differences between the computed and measured trajectories may be attributed to measurement errors, violation in the experiment of the equilibrium constraints, simplicity of the tire representation, and

omission of aerodynamic effects. The effect of some factors that could affect correlation is examined later.

Correlation of steered run.- For this test, the model touches down in a crabbed or yawed attitude ($\theta = 30^\circ$) with its gears aligned with the direction of motion ($\delta_i = -30^\circ$, $i = 1, 2, 3$). The main gears are fixed ($\delta_1 = \delta_3 = -30^\circ$) and the nose gear is steered by remote control. The initial conditions are as follows:

$$\dot{x}(0) = 6.81 \text{ m/sec}$$

$$\dot{y}(0) = 0 \text{ m/sec}$$

$$\dot{\theta}(0) = 30^\circ$$

$$\dot{\theta}(0) = 0 \text{ deg/sec}$$

For the numerical results, the measured nose-gear steering angle from reference 1 directly replaces the nose-gear swiveling degree of freedom in the equations of motion. The steering-angle input may be seen in figure 7 which presents the computed and measured trajectories for the early portion of this test. The analysis shows good correlation with experiment within the time range of comparison.

EFFECTS OF VEHICLE PARAMETERS AND INITIAL CONDITIONS

In this part of the paper, vehicle parameters and initial conditions are varied and the effects of their changes are demonstrated by displaying the computed trajectories of the unsteered-vehicle test of figure 6, both with and without parameters varied and by comparing final trajectory values. Effects of changes on a trajectory time-history variable are defined to be significant for the time period shown if final values of longitudinal distance, lateral distance, or heading angle differ from the basic test by at least 15 percent, 80 percent, or 30 percent, respectively.

Effects of Vehicle Parameters

In this section, parameters which relate to the mass properties, gear spacing, gear alignment, tire drag force, and time lag of the tire-force buildup are varied, and the effects are evaluated.

Mass properties.- The mass of the vehicle was varied with respect to the basic-test vehicle of figure 6. Because the tire side force varies nonlinearly with the normal gear load, some redistribution of tire side loads may be expected. Figure 8 shows the effect of reducing the vehicle mass to 90 and 80 percent of the basic test; the trajectory of the basic test is included in these studies for reference. Essentially no change in the longitudinal-distance time history is exhibited, and the mass reduction is shown to reduce the heading angle and lateral-distance excursions slightly.

The effect of shifting the vehicle c.g. longitudinally is shown in figure 9. For these runs, the vehicle c.g. is shifted about the nominal c.g. position, both forward and aft 3.2 percent of the nose-to-main-gear distance. Although the c.g. shift is small, the forward position does approximate a 20-percent aerodynamic-chord location for a representative aircraft. Figure 9 again shows essentially no change in the longitudinal-distance time history and slight changes in the lateral distance

and heading behavior as compared with results of the basic-vehicle test. Significant changes in the lateral distance and heading angle would be produced for a larger c.g. shift, such as a change in c.g. position of 10 percent of the nose-to-main-gear distance. Since the general-trajectory characteristics of figure 9 remain unchanged, the center of the lateral tire forces must be remaining forward of the vehicle c.g. for the c.g. variations. However, the figure shows that moving the c.g. forward reduces the heading change.

As shown in figure 10, a lateral shift of the c.g. also has a slight effect on the trajectory. For these computations, the c.g. position was offset from the vehicle center line ± 10 percent of the main-gear spacing. The trajectories show a reduced excursion magnitude of the model when the model c.g. is positioned to the right of the center line and an increased excursion magnitude for a left position.

A parameter that affects vehicle equilibrium is the vehicle c.g. elevation above the surface. Although not shown on a figure, a 10-percent height increase of the c.g. was found not to affect the trajectory time histories significantly.

Gear spacing.- The effects on the vehicle trajectories of longitudinal and lateral gear spacing were also studied. The trajectories shown in figure 11 are for a reduction in the longitudinal nose-to-main-gear distance of 20 and 40 percent of that of the basic vehicle. The effects on the trajectory are insignificant. In addition, results were computed with the lateral main-gear spacing halved and doubled. The trajectories are shown in figure 12, where the narrower spacing increased the lateral excursions, but again the effects were small.

Gear misalignment.- Gear misalignment may have a strong influence on the rollout trajectory of a vehicle. To indicate the relative sensitivity of nose and main-gear misalignment, calculations were made first with the nose gear misaligned $\pm 1^\circ$, and then with the left main gear misaligned $\pm 1^\circ$.

Figure 13 shows the effect of the nose-gear misalignment on the trajectory. The misalignment produced a significant effect on the lateral distance and heading time histories; and for the clockwise (positive) angle of misalignment, there was also a slight effect on the longitudinal distance behavior. The clockwise gear misalignment caused large lateral vehicle motions, and the 1° counterclockwise (negative) nose-gear rotation was sufficient to direct the vehicle downwind.

Figure 14 presents trajectories for $\pm 1^\circ$ misalignment of the left main gear. The data indicate trajectory characteristics similar to those for the nose-gear misalignment; however, the heading response is opposite to that for the nose-gear misalignment, and the vehicle response is less sensitive to main-gear alignment. For instance, figure 14 shows that a 1° main-gear misalignment nearly causes the vehicle to traverse a straight path. However, from interpolation of figure 13, a similar behavior could be achieved with a nose-gear-misalignment magnitude of about one-half of the main-gear misalignment.

Effect of tire drag force and its distribution.- Differential braking derived from unbalanced drag forces on the main gears of an aircraft is well known as an effective means of steering. Although wheel braking is not treated in this paper, a steering effect can occur because of unequal wheel or tire rolling resistances of each gear occurring as a result of wheel imperfections, differential gear loadings, or yaw angles. To indicate effects of tire drag, the drag of all of the wheels was reduced to zero and doubled. Trajectories for these conditions are shown in figure 15 where, as expected, the longitudinal-distance time history depicts significant

changes in slope and, hence, in model speed. When the left-main-gear drag is removed and doubled as shown in figure 16, there is little change in the longitudinal-distance time history but a significant change in the lateral and heading behavior. In view of this sensitivity, the main-gear drag forces of the basic run were averaged and reapplied equally to the main gears at each computing interval to verify that main-gear tire drag differences were not a significant influence. The resulting trajectory together with the basic trajectory are presented in figure 17; the effect on the basic trajectory was small as indicated by the small trajectory differences.

Effect of tire moment.- Tire side forces are the primary source of directional control of the model, but tire moments, occurring because the side force does not generally act at the wheel center, also affect the motion. To illustrate the effect of the tire moment on the basic trajectory, all tire moments were eliminated from the basic-trajectory computation and the resulting trajectory was compared with the basic trajectory in figure 18. The effect is small but the tire moment is shown to reduce model excursions.

Effect of tire-force-buildup lag.- In all computer runs, the tire side force and moment were delayed a short period of time to simulate more closely the kind of tire behavior that was experienced in references 5 and 6. The computed delay increased in duration with decreasing wheel rotation speed and was expected to be more significant for tests for which the tire yaw angles were large and changing abruptly. To demonstrate the effect of the lag, the basic run was first repeated with a tire-force-buildup distance decreased to zero and then was increased by a factor of four. The effect of the changes on the trajectory was imperceptible.

In summary, the computed results described in this section show little sensitivity of the model behavior to model mass, lateral c.g. position, lateral or longitudinal gear spacing, tire moment, and small shifts in the longitudinal c.g. position. There was no perceptible effect from the tire-force-buildup lag. On the other hand, the model behavior was sensitive to gear alignment and generally sensitive to tire drag.

In addition to these specific findings, the computed results of figures 8 to 18 show that the lateral motion of the model is strongly related to the heading behavior. None of the vehicle-parameter changes altered the general characteristic shapes of the trajectories, and the lateral and heading motions acted essentially independently of the longitudinal motion except when drag variations were significant.

Effect of Initial Conditions

The effect on vehicle trajectories of vehicle initial conditions, that is, longitudinal velocity, lateral velocity, heading angle, and rate of change of heading angle, is considered in this section.

Longitudinal velocity.- Figure 19 shows vehicle trajectories of the basic run and for the model with its longitudinal velocity $x(0)$ increased 25 and 50 percent. The computed longitudinal-distance time histories are characterized by significant changes in distance at 2.4 sec. The increased longitudinal velocity produces a more rapid divergence in the lateral and heading motion of the vehicle. It may be recalled that similar trajectories were computed for reduced tire drag, suggestive that much of the effect of drag on the trajectory of figure 15 was velocity related. Not shown in figure 19 is that for computer runs at speeds slightly above the

50-percent speed increase, the right-main-gear normal force approached zero, implying that vehicle overturning was imminent.

Lateral velocity.- Effects of an initial lateral velocity $y(0)$ of ± 10 percent of the longitudinal velocity were imposed on the vehicle. The effects on the trajectory are shown in figure 20. The initial lateral velocity significantly affected the lateral-distance and heading-angle time histories but had minimal effect on the longitudinal distance. The downwind (negative) lateral velocity causes the vehicle to drift downwind more than for the basic run, but then the vehicle diverges at a faster rate in the upwind direction.

The upwind (positive) lateral velocity altered the characteristic shapes of both the heading-angle and lateral-displacement response curves. The lateral-distance time history shows that the vehicle first swings upwind then downwind before the vehicle started its eventual upwind excursion. Concurrently, the heading-angle time history also shows a brief downwind heading excursion before the vehicle headed upwind. These runs demonstrate the character of the tire side force to resist lateral motion of the model and to respond in heading to the forward-tire side-force center position.

Heading angle.- The effect of a $\pm 1^\circ$ heading misalignment at touchdown on the trajectory is shown in figure 21. The small heading misalignment influenced the lateral and heading behavior only slightly and the longitudinal-distance time history imperceptibly. The initial 1° clockwise or upwind (positive) vehicle rotation was sufficient to overcome the downwind lateral drift of the basic run and caused the vehicle to diverge at a faster rate in the upwind direction. An initial counter-clockwise (negative) heading promoted a longer and deeper downwind lateral excursion.

Heading-angle rates of change.- Heading-angle rates of change of ± 4 deg/sec were imposed on the basic-vehicle run; the resulting trajectories are presented in figure 22. A comparison of figures 21 and 22 shows that the trajectories of figure 22 are quite similar to those for an initial heading misalignment, except that there is no initial heading-angle offset.

CONCLUDING REMARKS

Planar equations of rollout motion have been derived for an aircraft in a three-point attitude subjected to applied forces and moments and having freely castoring or steerable landing gears equipped with pneumatic tires. The applied lateral and longitudinal forces and yawing moments which may be due to aerodynamics, engine thrust, and runway slope were resisted by tire action. Unsteady tire forces were improvised from steady-state force data by introducing a time lag between the tire yaw angle and the attendant tire force. Gear loads normal to the runway were determined from equilibrium conditions assumed about the roll and pitch axes of the vehicle and normal to the runway surface. The equations of motion have been programmed and numerically integrated on a high-speed digital computer to describe the position and heading of an aircraft relative to a fixed-runway coordinate-axis system.

Results from the equations were first compared with two experimental trajectories of a small landing-gear model. In these tests, the model traversed a laterally sloping runway that simulated a crosswind, and the model main gears were fixed and the nose gear was either fixed or lightly steered. The computed analytical trajectories were in good agreement with the experimental trajectories.

Studies were also conducted to show the effect of various parameter changes on the vehicle trajectory. The trajectories were found to be particularly sensitive to angular gear misalignments, initial translatory velocities, and tire drag forces; lesser sensitivities were found for changes in mass, center-of-gravity positions, gear spacing, and rotational initial conditions. The effect of the force-buildup time lag for the rolling tire was insignificant for these tests.

Langley Research Center
National Aeronautics and Space Administration
Hampton, VA 23665
March 16, 1982

APPENDIX

FRICITIONAL PROPERTIES OF AN UNBRAKED, 11.4-CM DIAMETER,
PNEUMATIC MODEL-AIRPLANE TIRE

One of the landing gears of reference 1 equipped with a pneumatic tire was installed in a fixture to test for tire frictional properties on a drum dynamometer. The tire was an 11.4-cm-diameter hobby-type model-airplane tire inflated to a nominal pressure of 60 kPa. The dynamometer-drum diameter was 1.67 m, and the drum was covered with wood veneer to simulate the plywood surface described in reference 1. A photograph of the test setup is shown in figure A1. Tire forces consisting of the drag force F_D in the plane of the wheel, the side force F_S normal to the wheel plane, and the moment M_N about the vertical axis through the wheel center were measured for fixed (nominal) vertical loads F_N of 28.6, 50.2, 71.8, and 93.3 N and fixed (nominal) yaw angles ψ of 0° , 3° , 6° , and 8.5° ; drum surface speeds ranged from 0.6 to 10.7 m/sec.

The results showed that the tire side force and moment were primarily sensitive to only normal loadings and yaw angles. For the conditions investigated, surface speed had little effect on the tire forces and, hence, its effect was disregarded from further consideration. The drag force was found to vary irregularly with normal load and yaw angle as shown in table AI.

For constant normal loads and different yaw angles, the tire side forces were found to be nearly proportional to the yaw angle, and for more general applicability, a tire side-force parameter was formulated by normalizing the side force to the yaw angle. This parameter is computed for all normal loads and test conditions and is displayed as a function of the normal load in figure A2, where the experimental data are denoted by symbols in the figure and the units of the yaw angle ψ are expressed in degrees. The data show that the side-force parameter increases directly with the normal load for low values and approaches a limiting value as the load increases. Such a relationship has been curve fitted to an exponential function by using a least-squares approximation for its coefficients and is given for the model tire by

$$\frac{F_S}{\psi} = -5.01 \left(1 - e^{-0.0422F_N} \right) \quad (A1)$$

where the units of the angle ψ are given in degrees and the units of the forces F_S and F_N are given in newtons.

The tire moment M_N found in the tests for each of the four different normal loadings is shown in figure A3 as a function of the yaw angle. As seen from equation (48) which is repeated here, a function of the form

$$M_N = -a_1(F_N) \left[1 - e^{-a_2(F_N)|\psi|} \right] \text{sgn}(\psi)$$

is assumed and the coefficients a_1 and a_2 are given by the curves of figure A4.

APPENDIX

TABLE AI.- APPROXIMATE DRAG FORCE FOR UNBRAKED MODEL-AIRPLANE TIRE

Yaw angle, ψ , deg	Normal force, F_N , N	Drag force, F_D , N
0	28.62	1.82
3.0	28.62	.00
6.0	28.62	.93
8.5	28.62	1.82
0	50.20	2.76
3.0	50.20	.93
6.0	50.20	.00
8.5	50.20	.93
0	71.76	3.65
3.0	71.76	1.82
6.0	71.76	1.82
8.5	71.76	.93
0	93.33	4.14
3.0	93.33	3.65
6.0	93.33	1.82
8.5	93.33	2.76

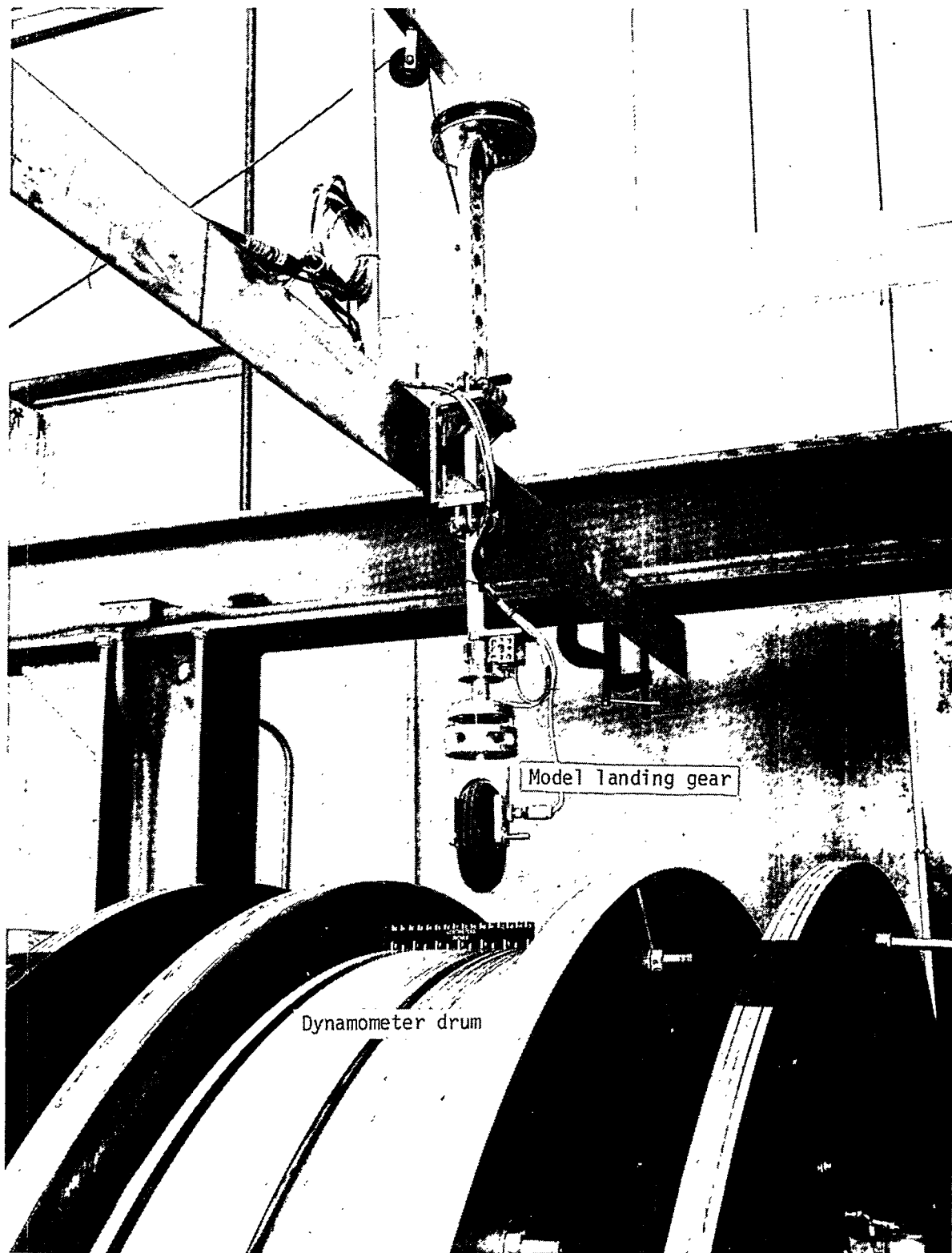


Figure A1.- Photograph of instrumented model landing gear and dynamometer drum.

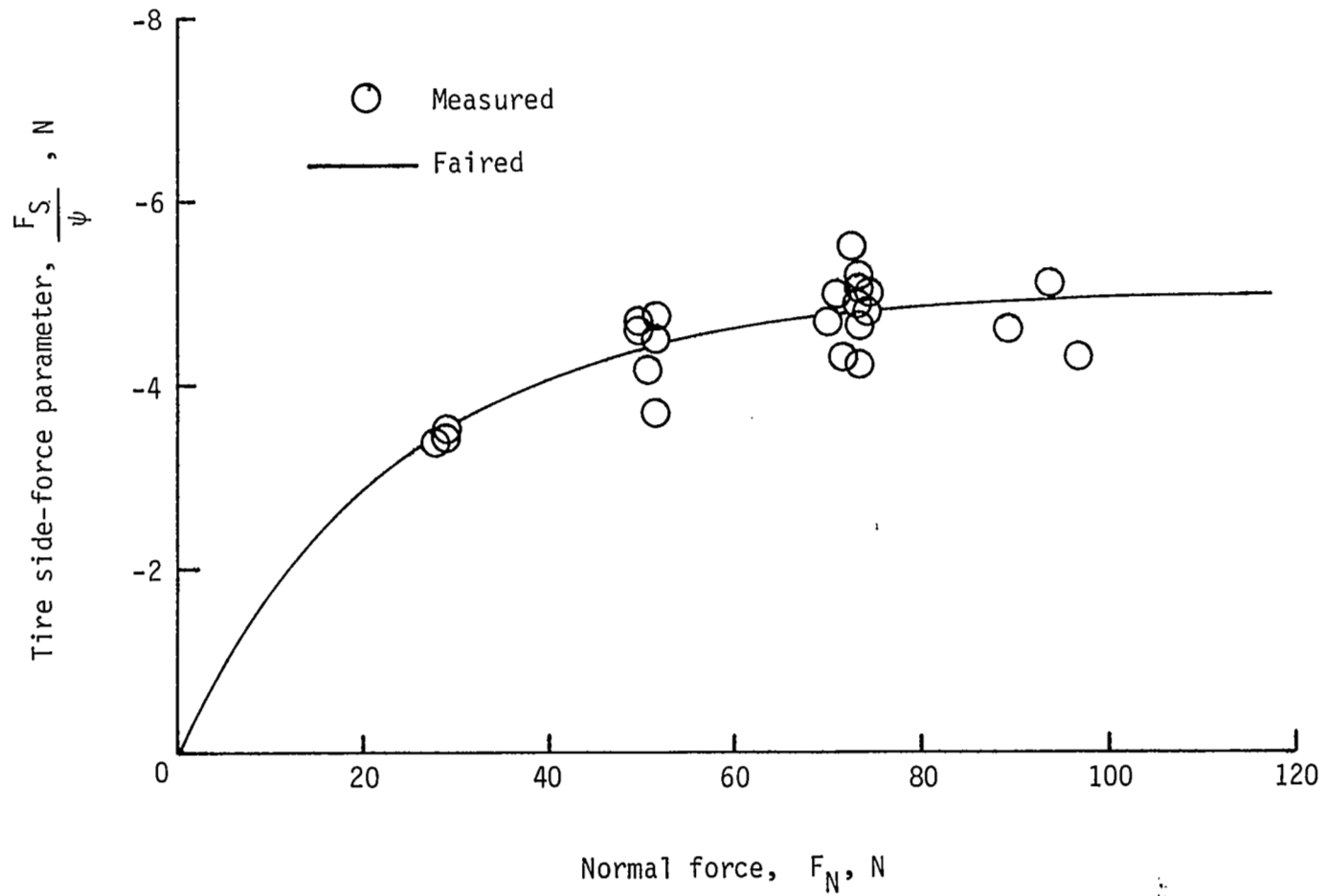


Figure A2.- Variation of tire side-force parameter with normal force for pneumatic model-airplane tire. Units of ψ are given in degrees.

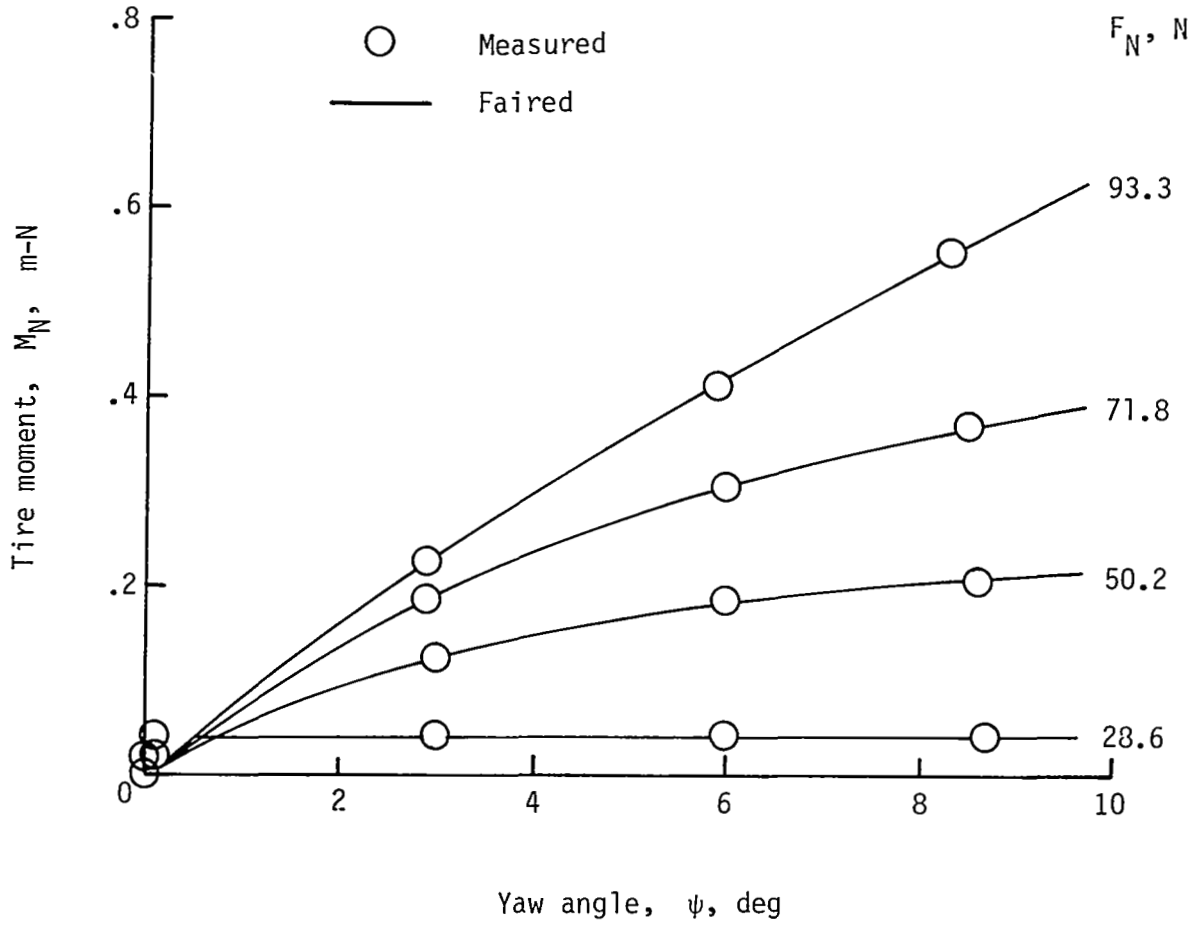


Figure A3.- Variation of tire moment with yaw angle and normal force for pneumatic model-airplane tire.

APPENDIX

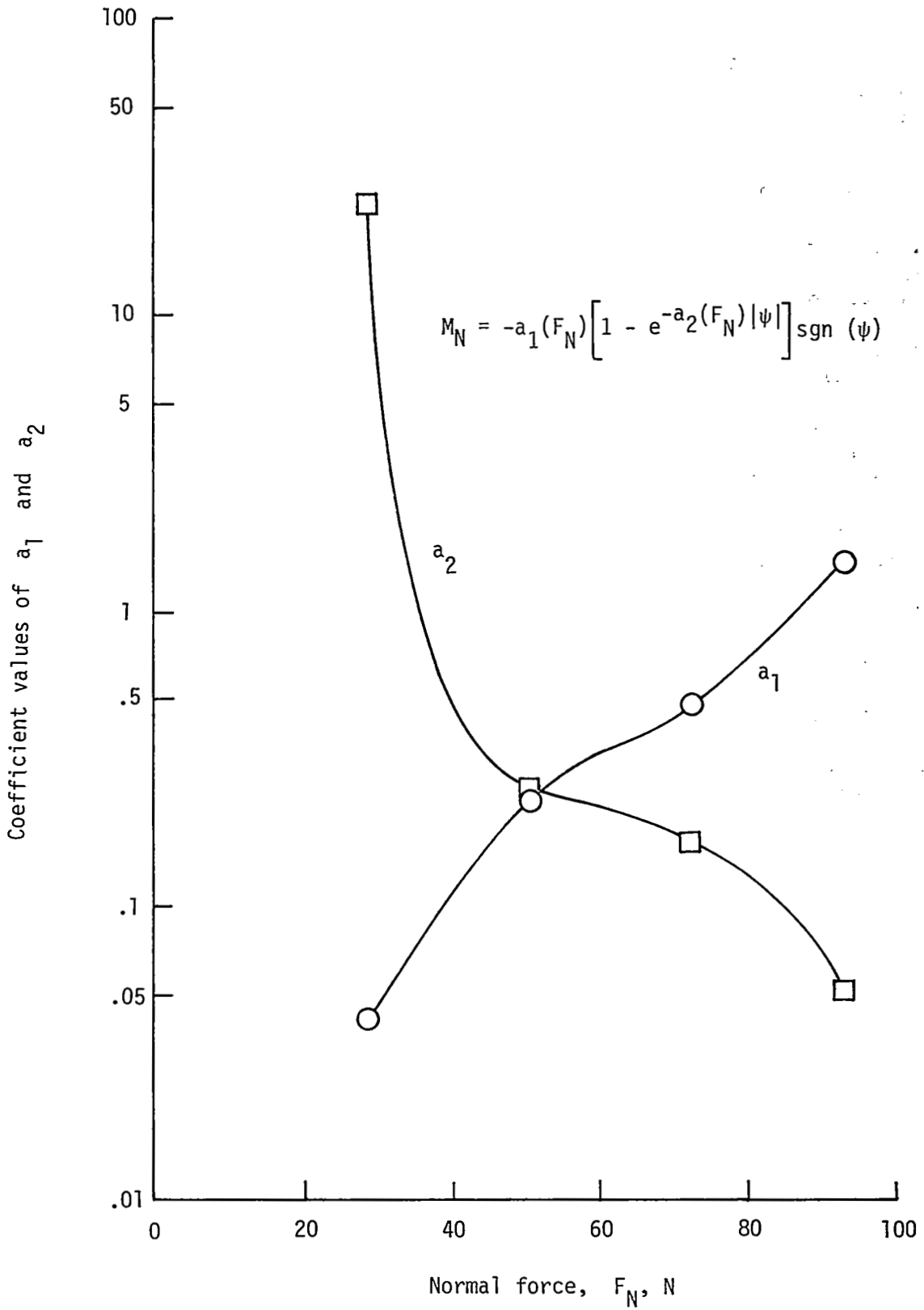


Figure A4.- Variation of coefficients of tire moment function M_N with normal force. Units of a_1 and M_N are given in meters-newtons, a_2 is dimensionless, and units of ψ are given in degrees.

REFERENCES

1. Stubbs, Sandy M.; Byrdson, Thomas A.; and Sleeper, Robert K.: An Experimental Simulation Study of Four Crosswind Landing-Gear Concepts. NASA TN D-7864, 1975.
2. Paslay, P. R.; and Slibar, A.: The Motion of Automobiles in Unbanked Curves. Ing.-Arch., vol. 24, no. 6, Nov. 1956, pp. 412-424.
3. Segel, Leonard: Theoretical Prediction and Experimental Substantiation of the Response of the Automobile to Steering Control. Proc. Auto. Div. Inst. Mech. Eng. (London), vol. 7, pt. 2A, 1956, pp. 310-330.
4. Hauer, Ezra: Determination of Wheel Trajectories. J. Transp. Eng., American Soc. Civil Eng., vol. 96, no. TE4, Nov. 1970, pp. 463-470.
5. Smiley, Robert F.; and Horne, Walter B.: Mechanical Properties of Pneumatic Tires With Special Reference to Modern Aircraft Tires. NASA TR R-64, 1960. (Supersedes NACA TN 4110.)
6. Bergman, Walter; and Beauregard, Claude: Transient Tire Properties. [Preprint] 740068, Soc. Automot. Eng., Feb.-Mar. 1974.
7. Sleeper, Robert K.; and Smith, Eunice G.: A Transformation Method for Deriving, From a Photograph, Position and Heading of a Vehicle in a Plane. NASA TN D-8201, 1976.
8. Goldstein, Herbert: Classical Mechanics. Addison-Wesley Pub. Co., Inc., c.1959.
9. Scanlan, Robert H.; and Rosenbaum, Robert: Introduction to the Study of Aircraft Vibration and Flutter. Macmillan Co., c.1951.
10. Clark, Samuel K., ed.: Mechanics of Pneumatic Tires. NBS Monogr. 122, U.S. Dep. Commer., Nov. 1971.

TABLE I.- MODEL MASS AND CONFIGURATION PROPERTIES

(a) Body

m_b , kg	16.46
I_b , kg-m^2	3.06
ξ_b , m	-0.0298
h , m	0.268

(b) Gears

Property	Gear position at index number -		
	Left at $i = 1$	Nose at $i = 2$	Right at $i = 3$
$m_{g,i}$, kg	1.034	1.034	1.034
$m_{w,i}$, kg	0.221	0.221	0.221
$I_{g,i}$, kg-m^2	0.000843	0.000843	0.000843
$I_{w,i}$, kg-m^2	0.000191	0.000191	0.000191
$\xi_{g,i}$, m	-0.0810	0.5633	-0.0810
$\eta_{g,i}$, m	-0.1854	0	0.1854
$\rho_{g,i}$, m	0.00427	0.00427	0.00427
$\rho_{w,i}$, m	0	0	0

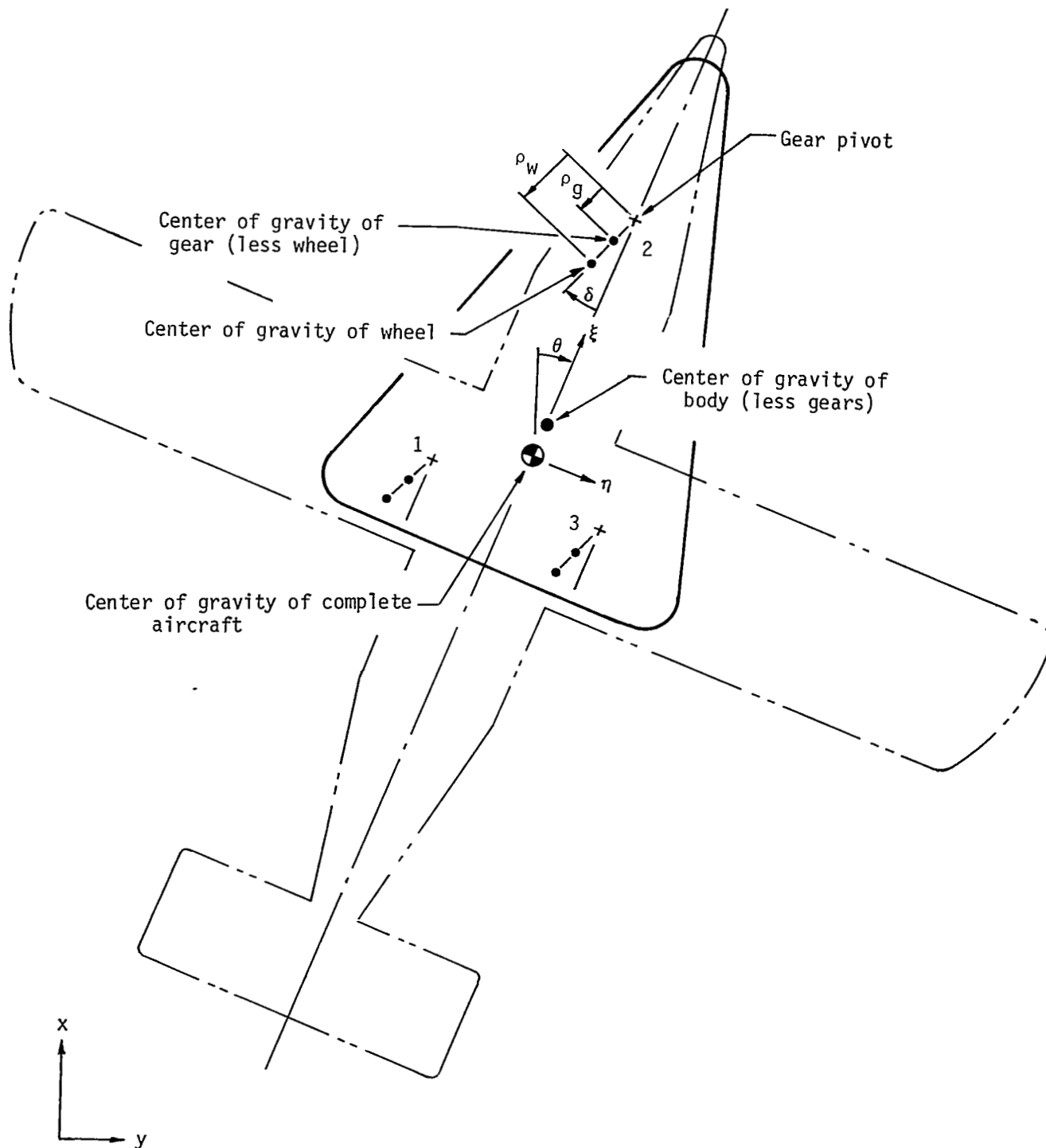


Figure 1.- Schematic representation of aircraft and its landing-gear system.

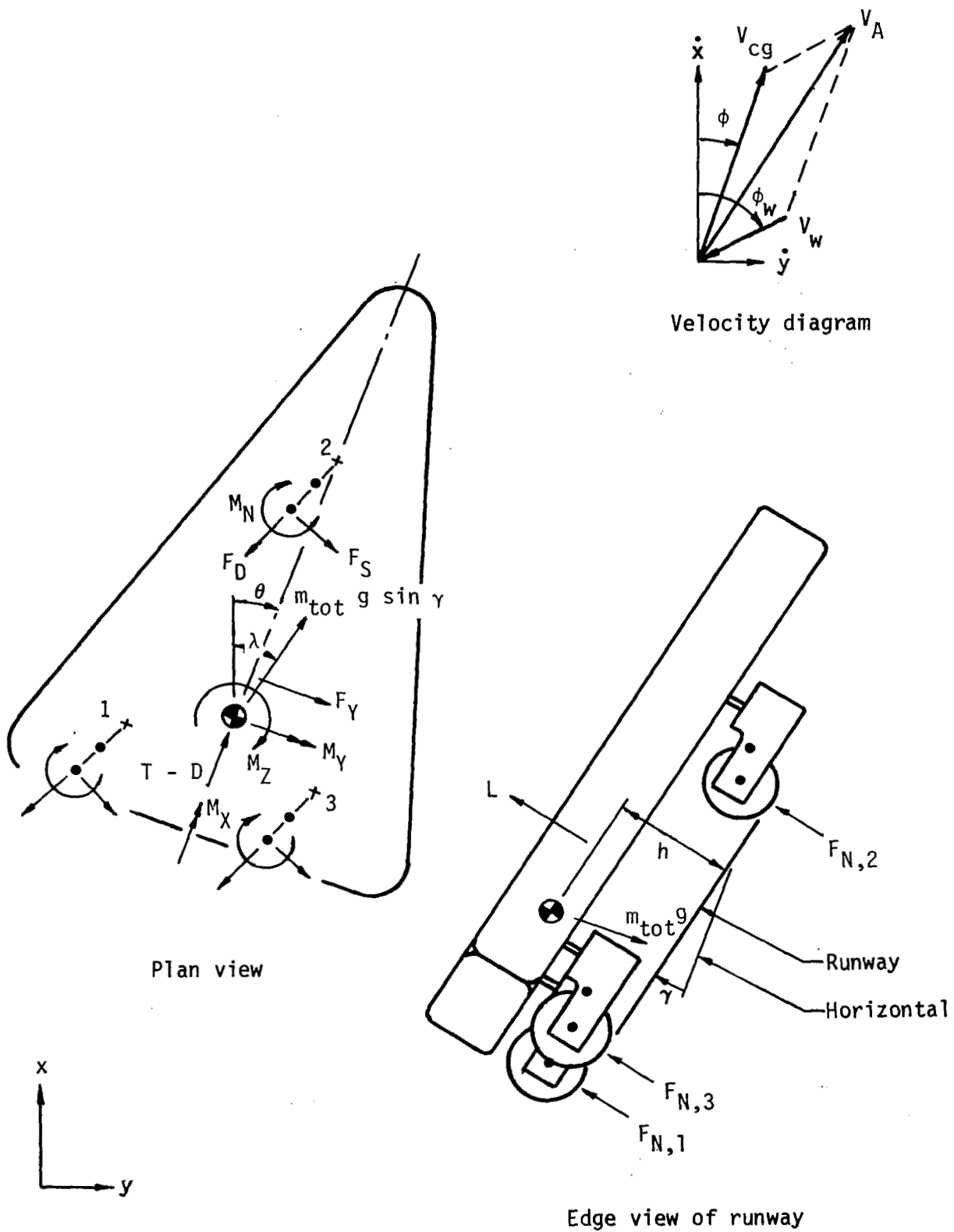
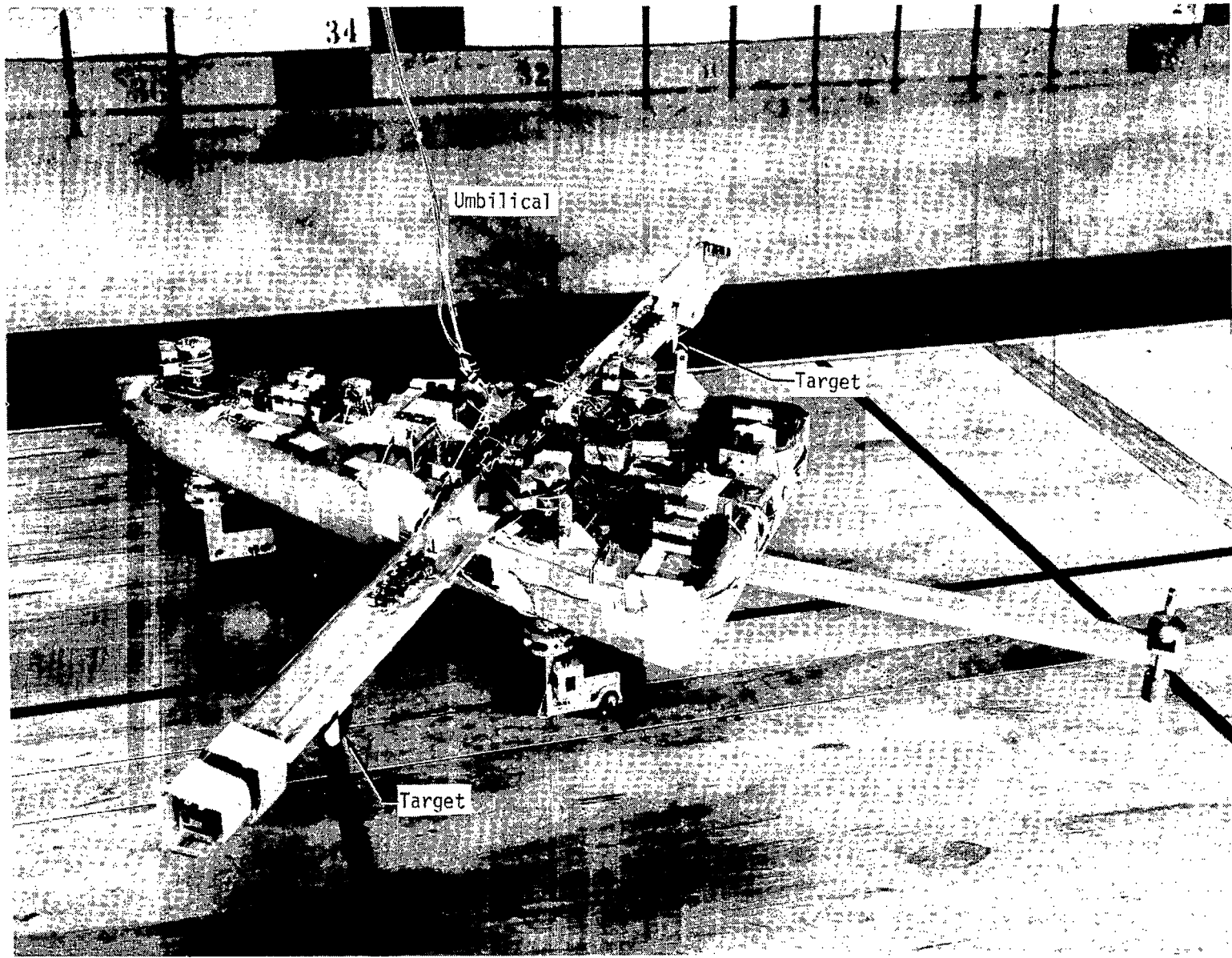
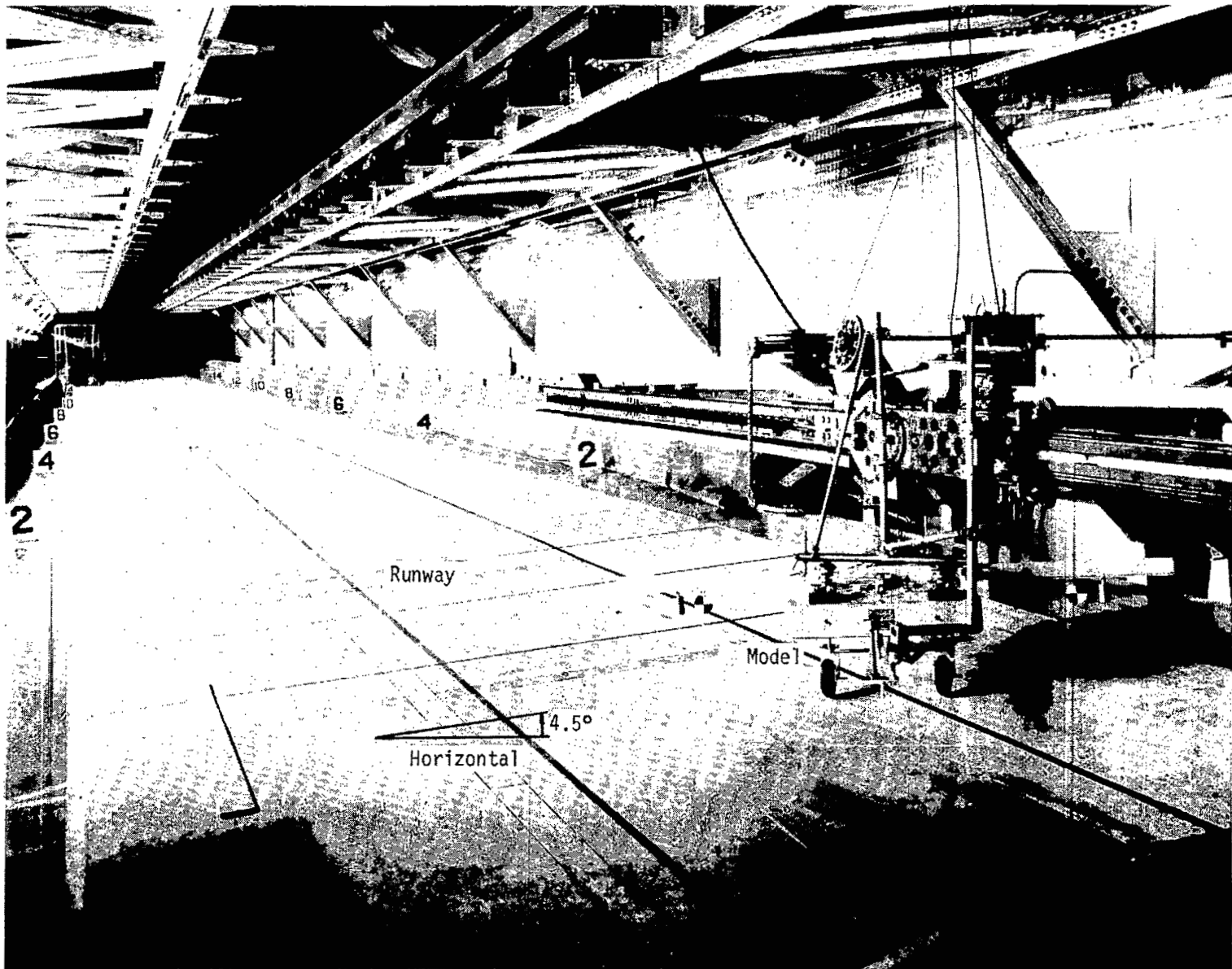


Figure 2.- Forces and moments applied to the aircraft.



L-73-5475.2

Figure 3.- Photograph of aircraft landing-gear model.



L-73-757.2

Figure 4.- Photograph showing view of aircraft landing-gear model on sloped runway.

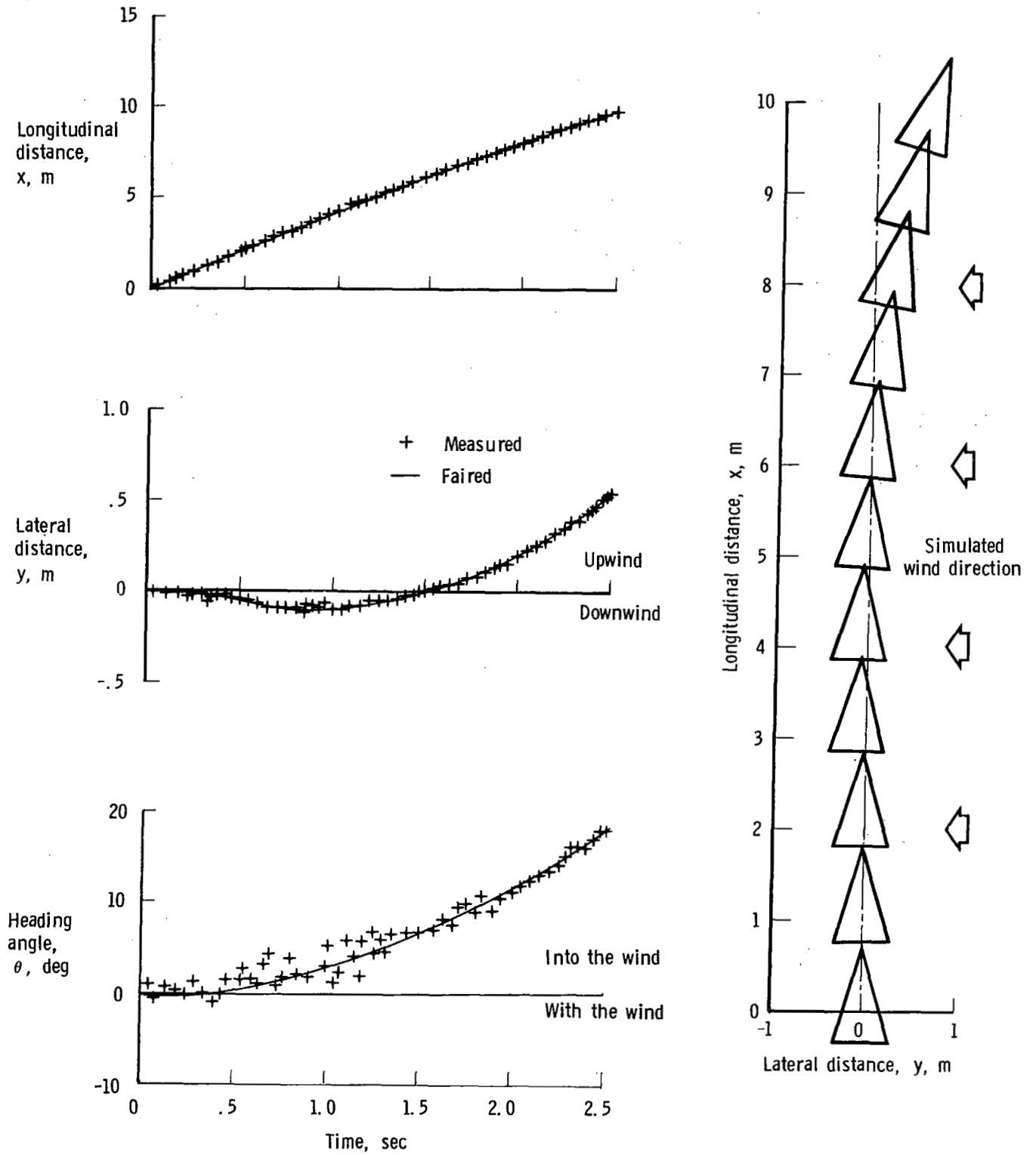


Figure 5.- Time histories and spatial display of experimental trajectory variables for unsteered model test.

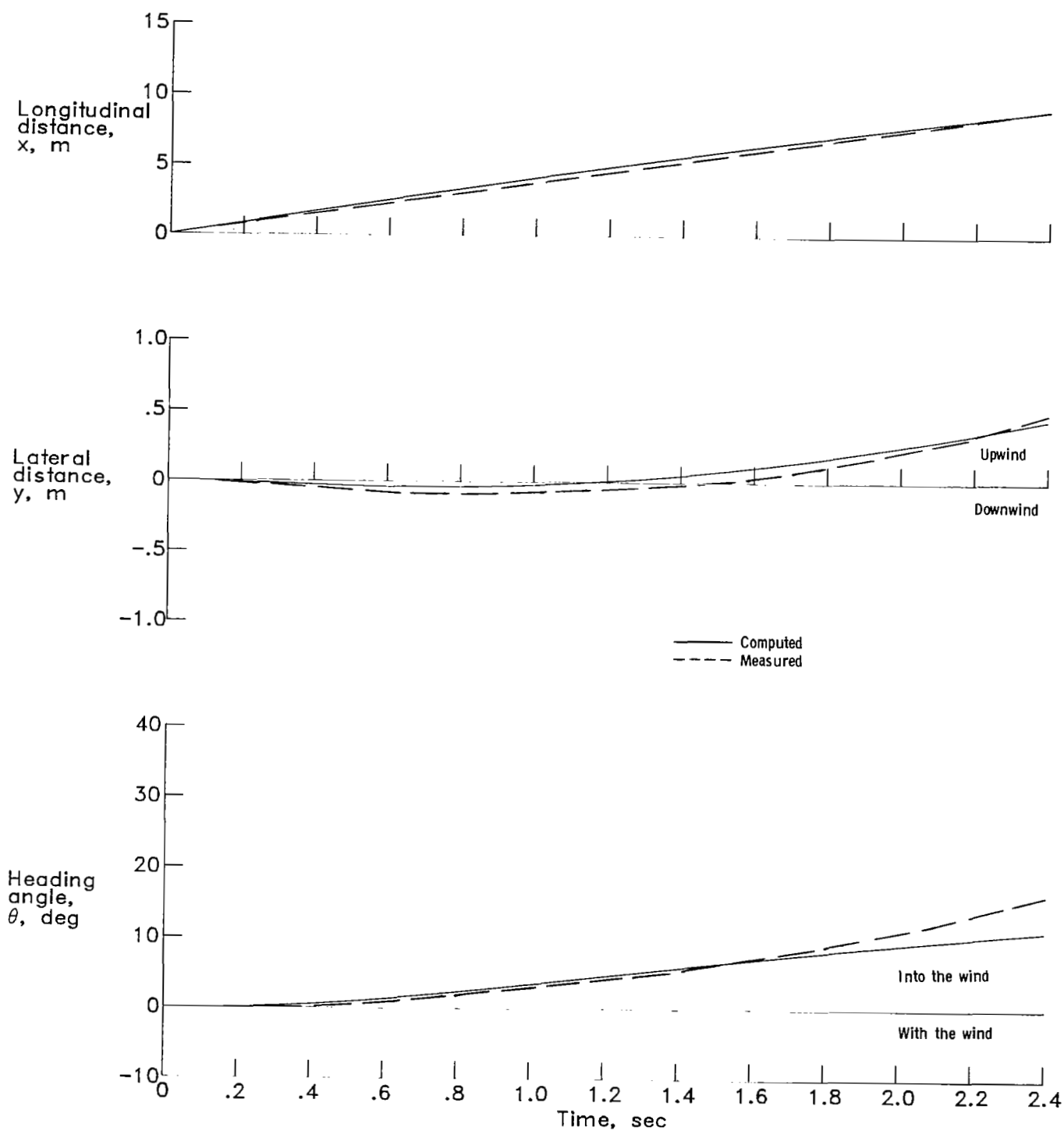


Figure 6.- Measured and computed trajectory-variable time histories for unsteered model test with touchdown variable $\dot{x}(0) = 4.41$ m/sec.

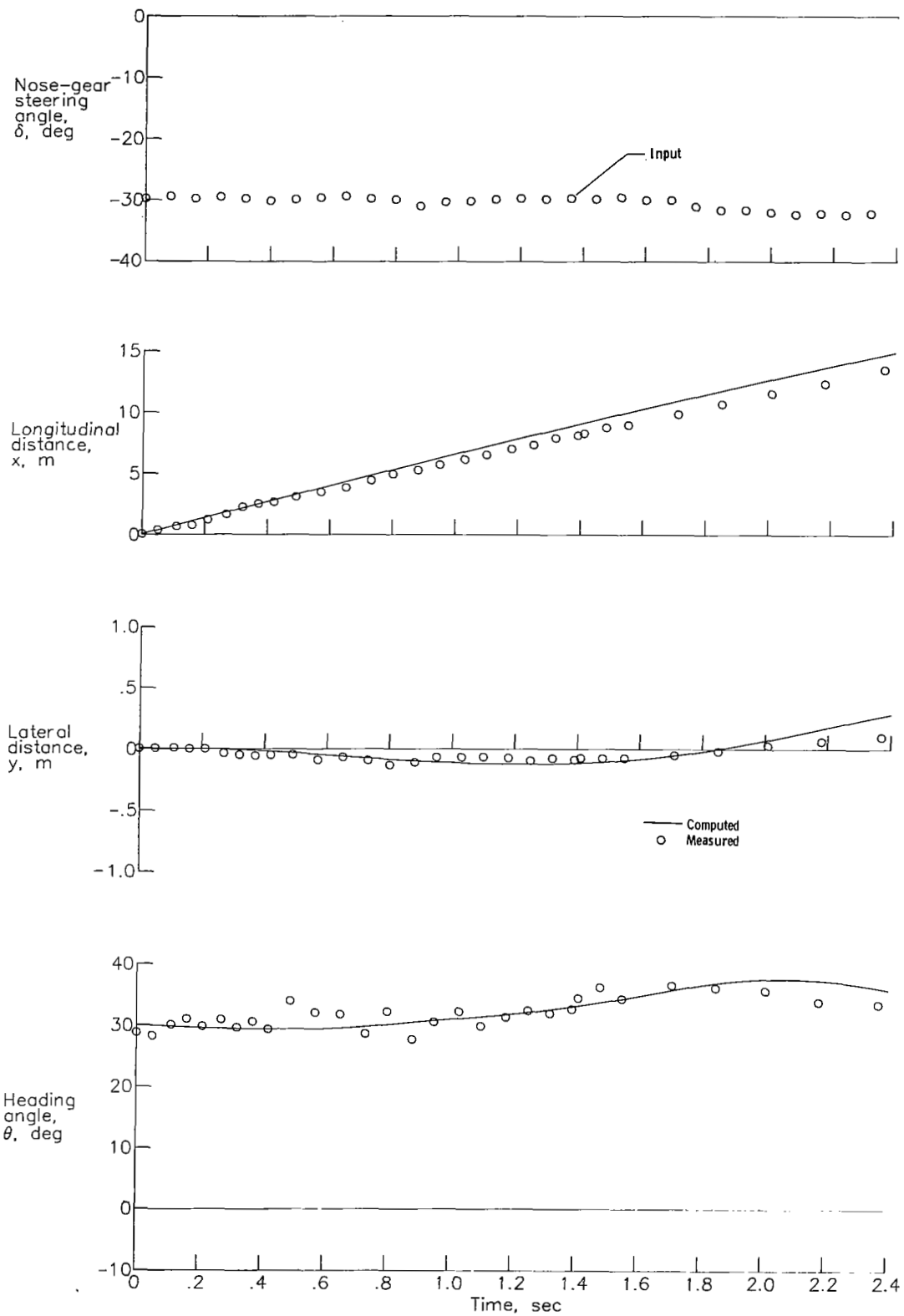


Figure 7.- Measured and computed trajectory-variable time histories for steered test of model with touchdown variables $\dot{x}(0) = 6.81$ m/sec and $\theta(0) = 30^\circ$.

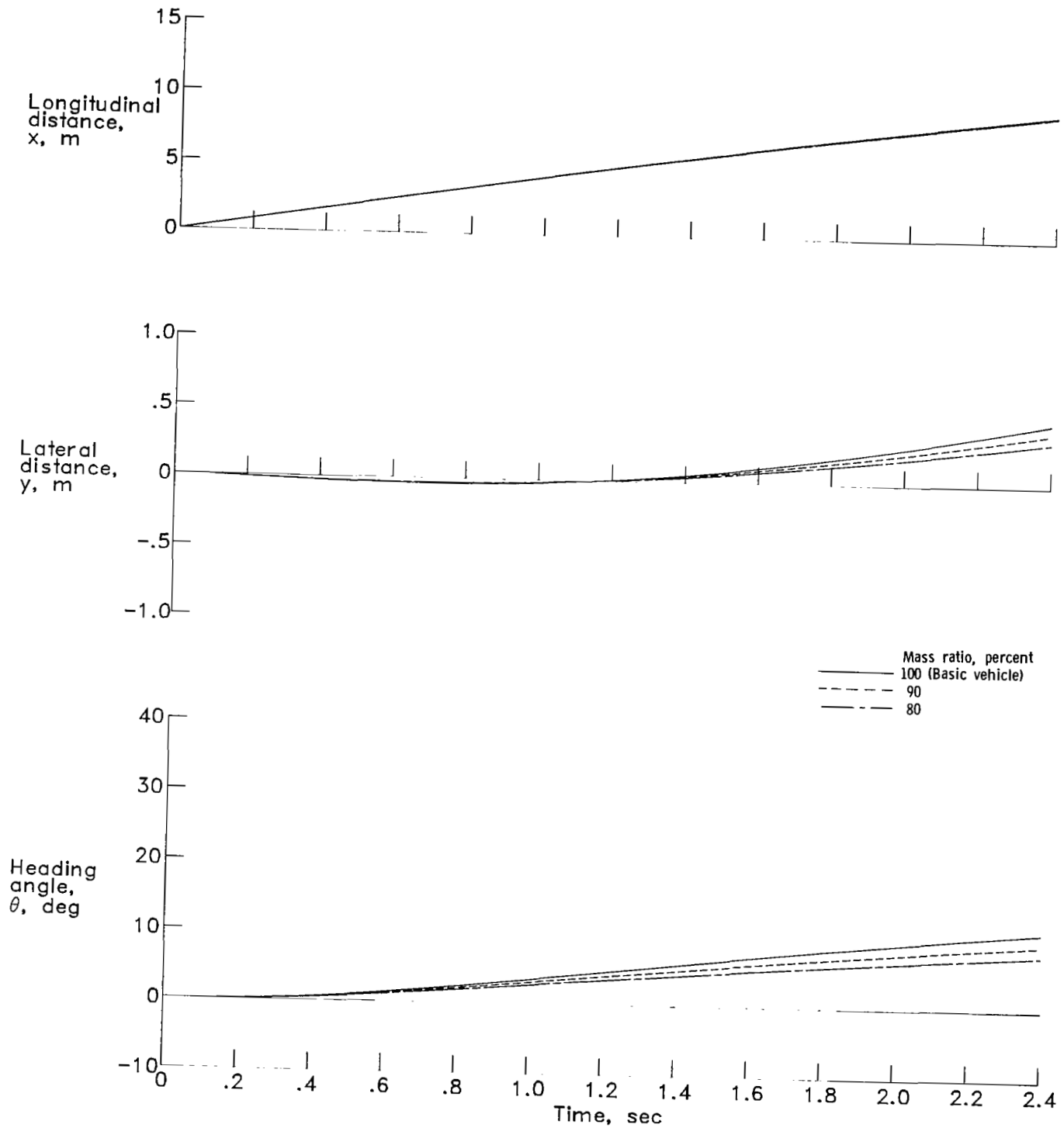


Figure 8.- Computed trajectory-variable time histories of basic vehicle with reduced mass.

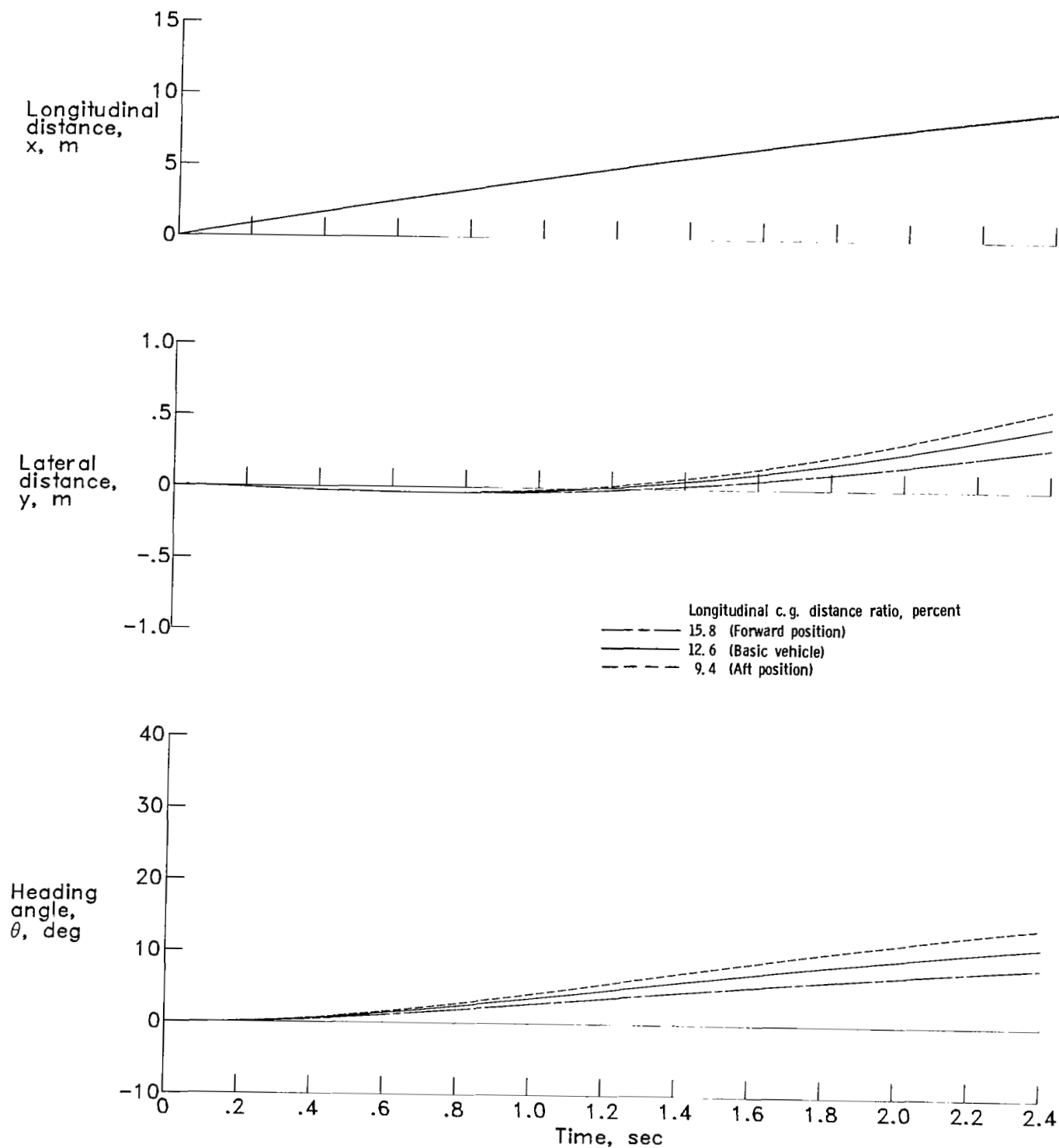


Figure 9.- Computed trajectory-variable time histories of basic-vehicle test with body center of gravity shifted longitudinally. Distance ratio is referred to the nose-to-main-gear spacing and is measured forward of the main gear.

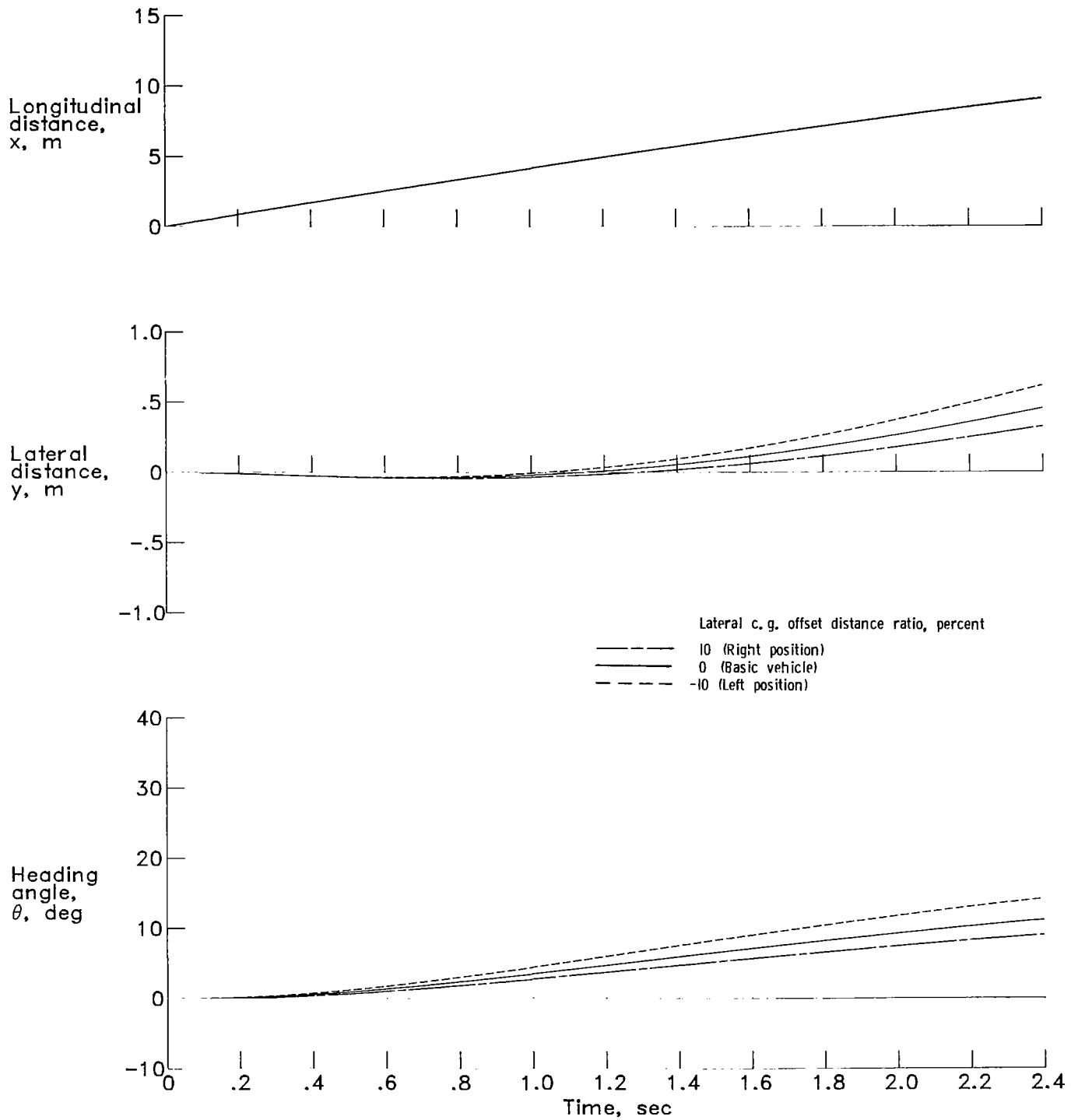


Figure 10.- Computed trajectory-variable time histories of basic vehicle with body center of gravity shifted laterally. Offset distance ratio is referred to main-gear spacing.

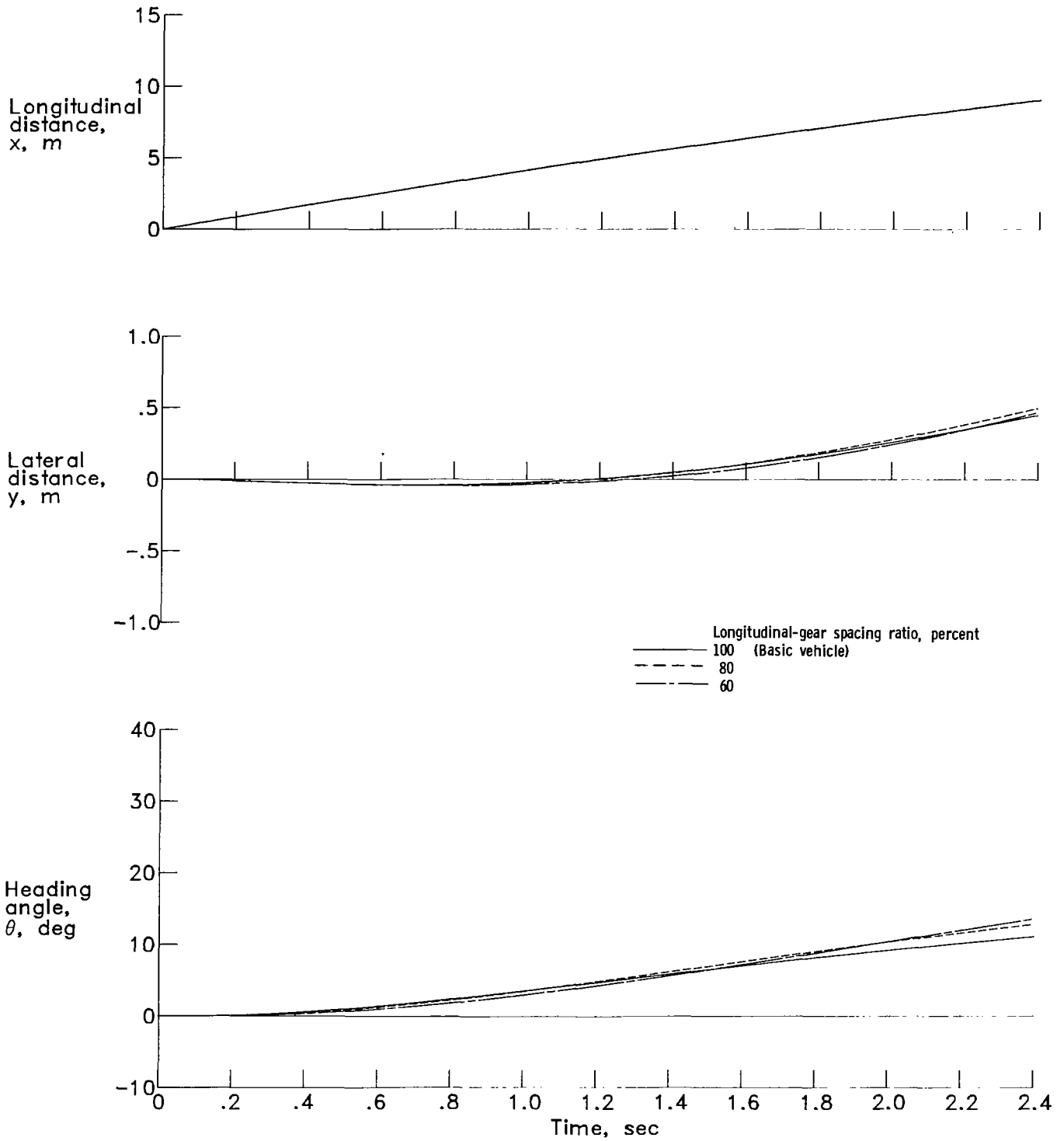


Figure 11.- Computed trajectory-variable time histories of basic-vehicle test with reduced nose-to-main-gear spacing.

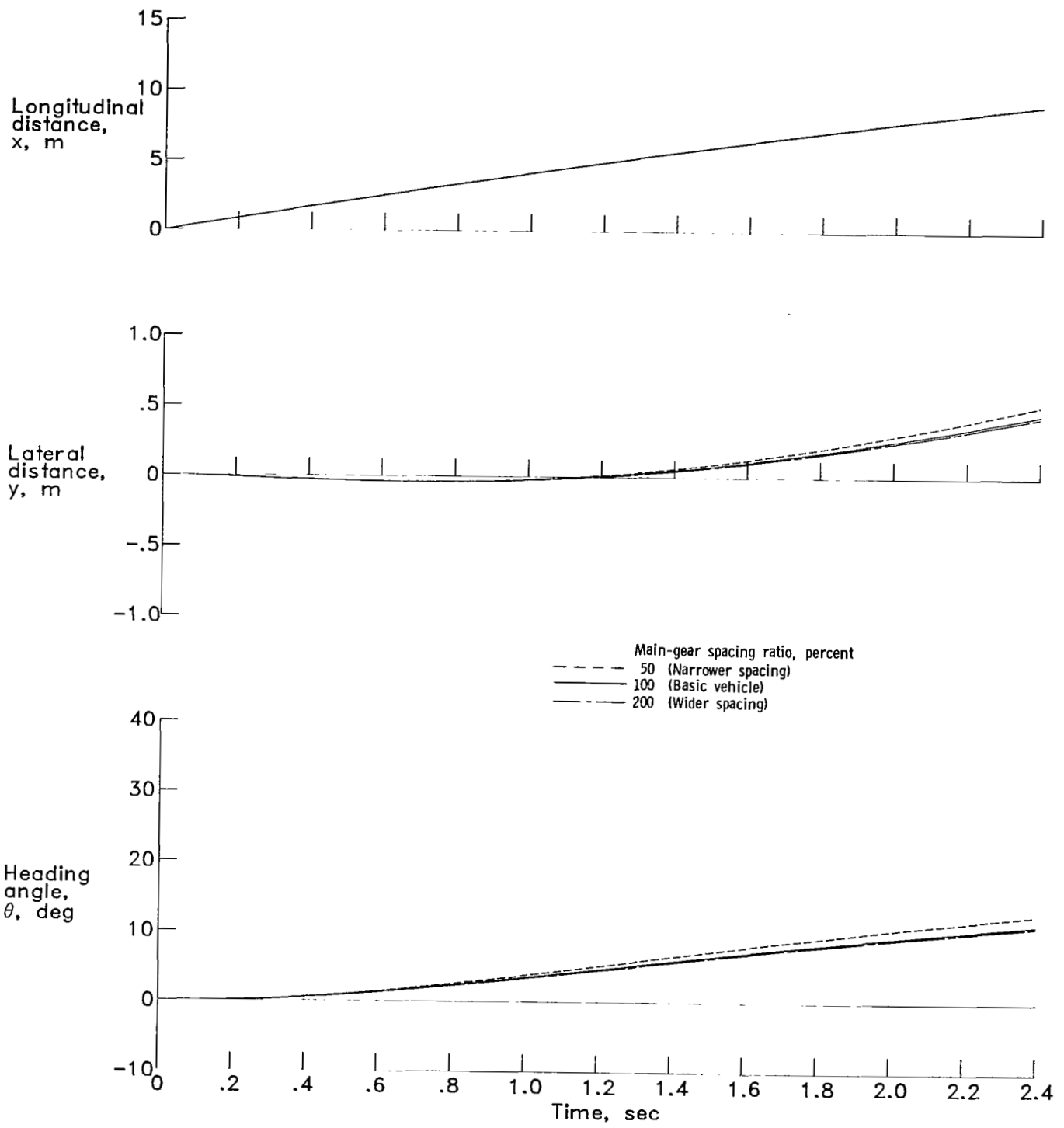


Figure 12.- Computed trajectory-variable time histories of basic-vehicle test with varied lateral main-gear spacing.

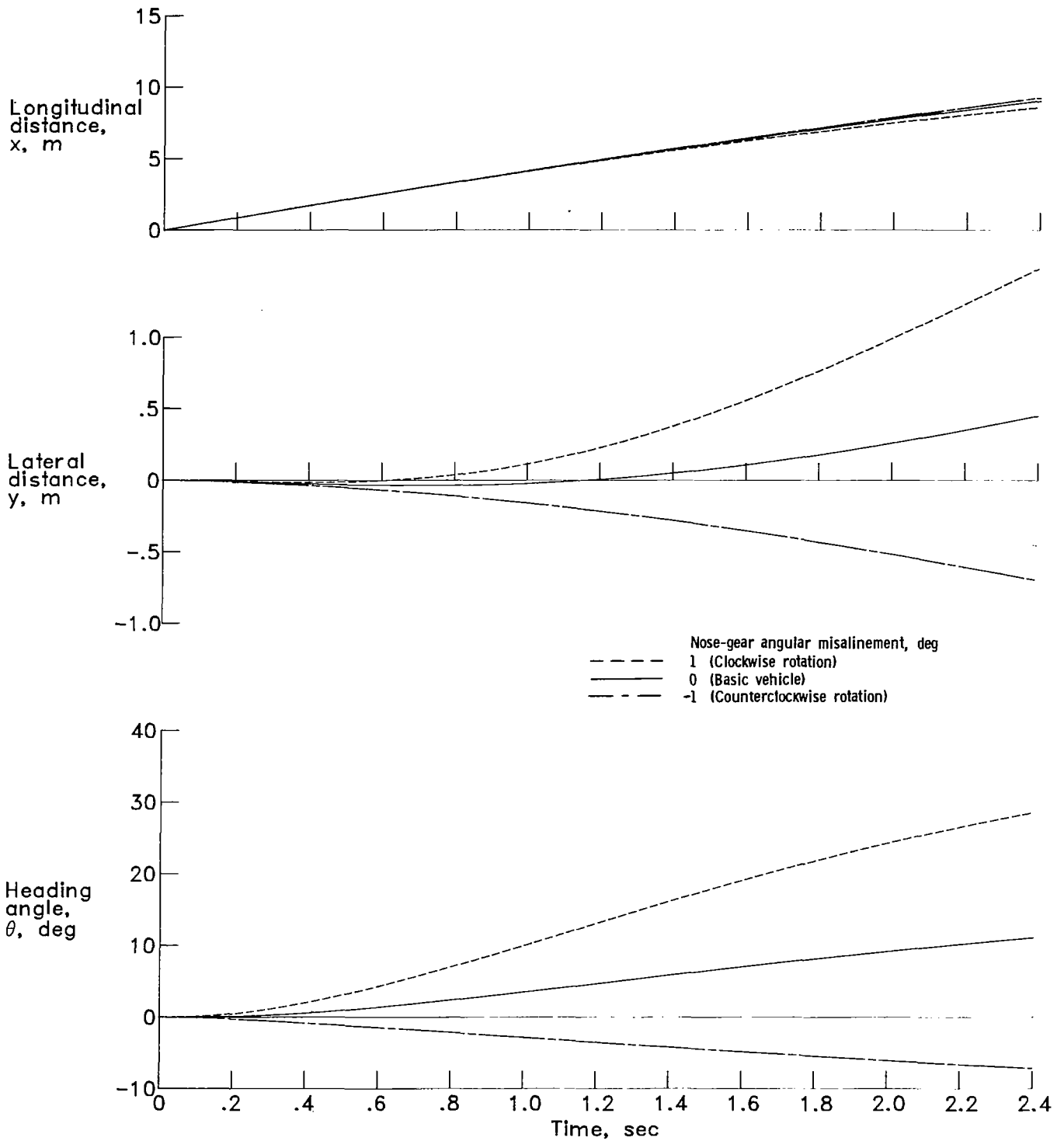


Figure 13.- Computed trajectory-variable time histories of basic-vehicle test with nose-gear misalignments.

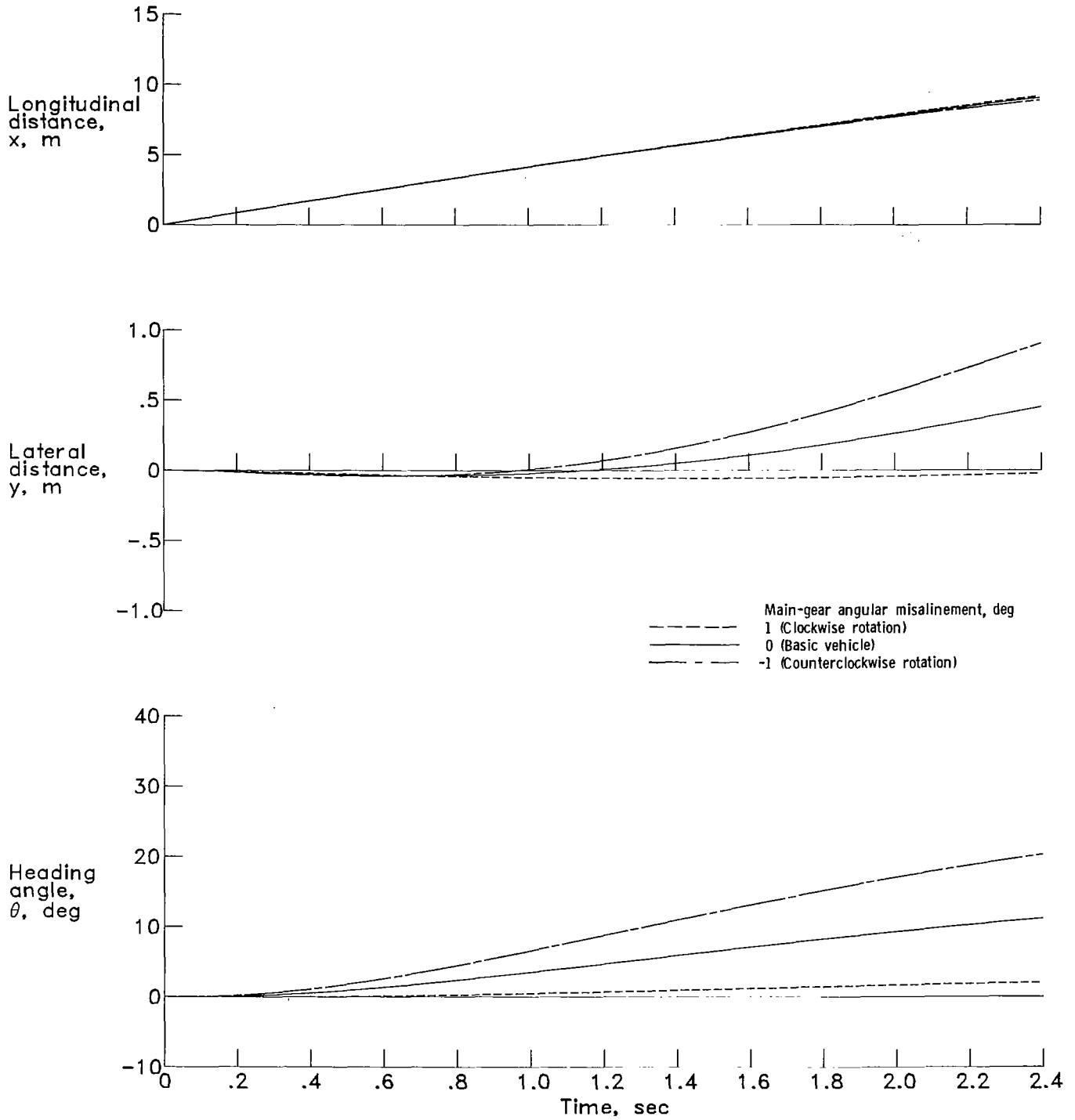


Figure 14.- Computed trajectory-variable time histories of basic-vehicle test with left-main-gear misalignments.

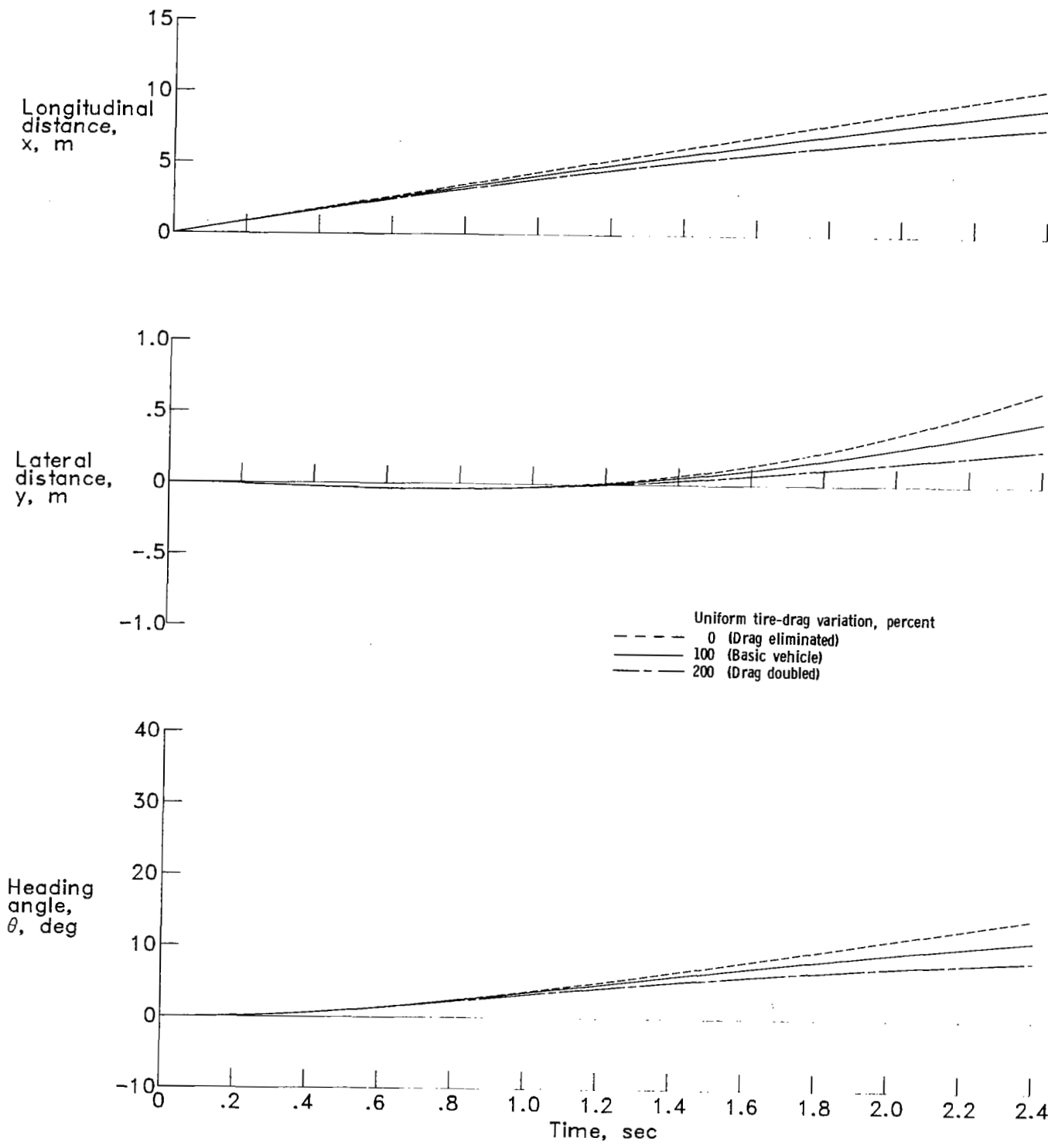


Figure 15.- Computed trajectory-variable time histories of basic-vehicle test with tire drag to all gears uniformly varied.

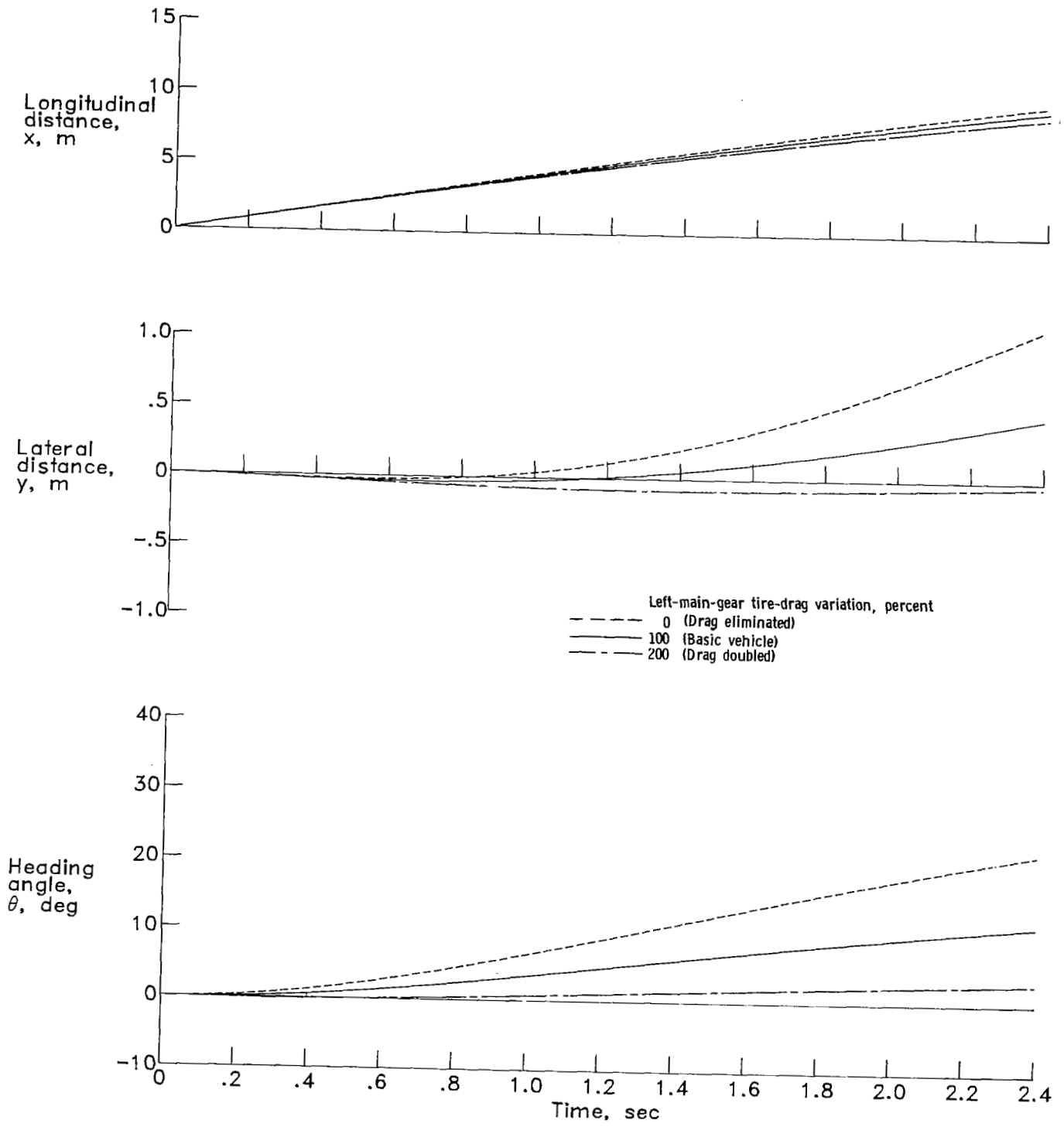


Figure 16.- Computed trajectory-variable time histories of basic-vehicle test with left-main-gear tire drag varied.

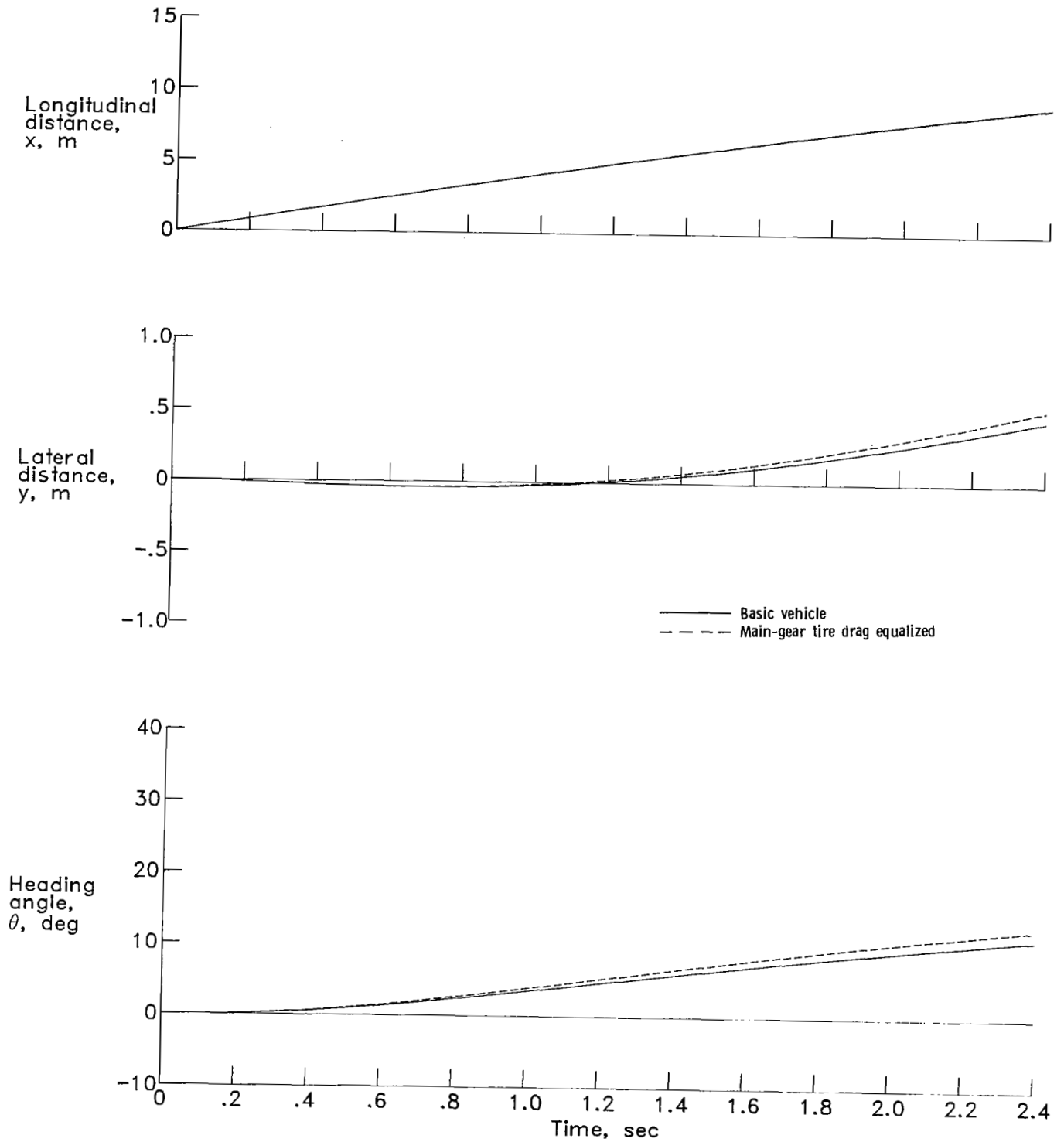


Figure 17.- Computed trajectory-variable time histories of basic-vehicle test with main-gear tire drag equalized to average values.

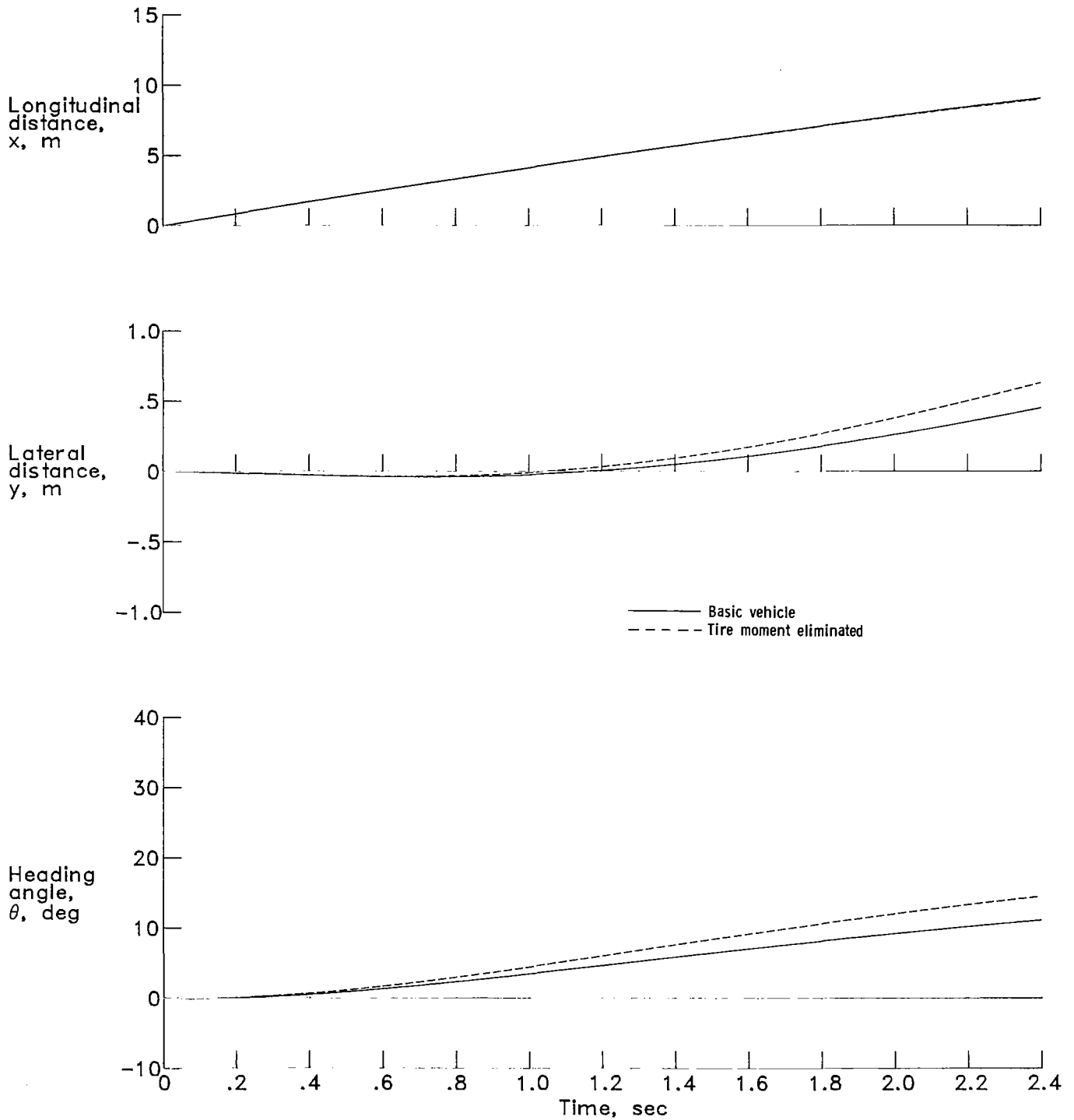


Figure 18.- Computed trajectory-variable time histories of basic-vehicle test without tire moment.

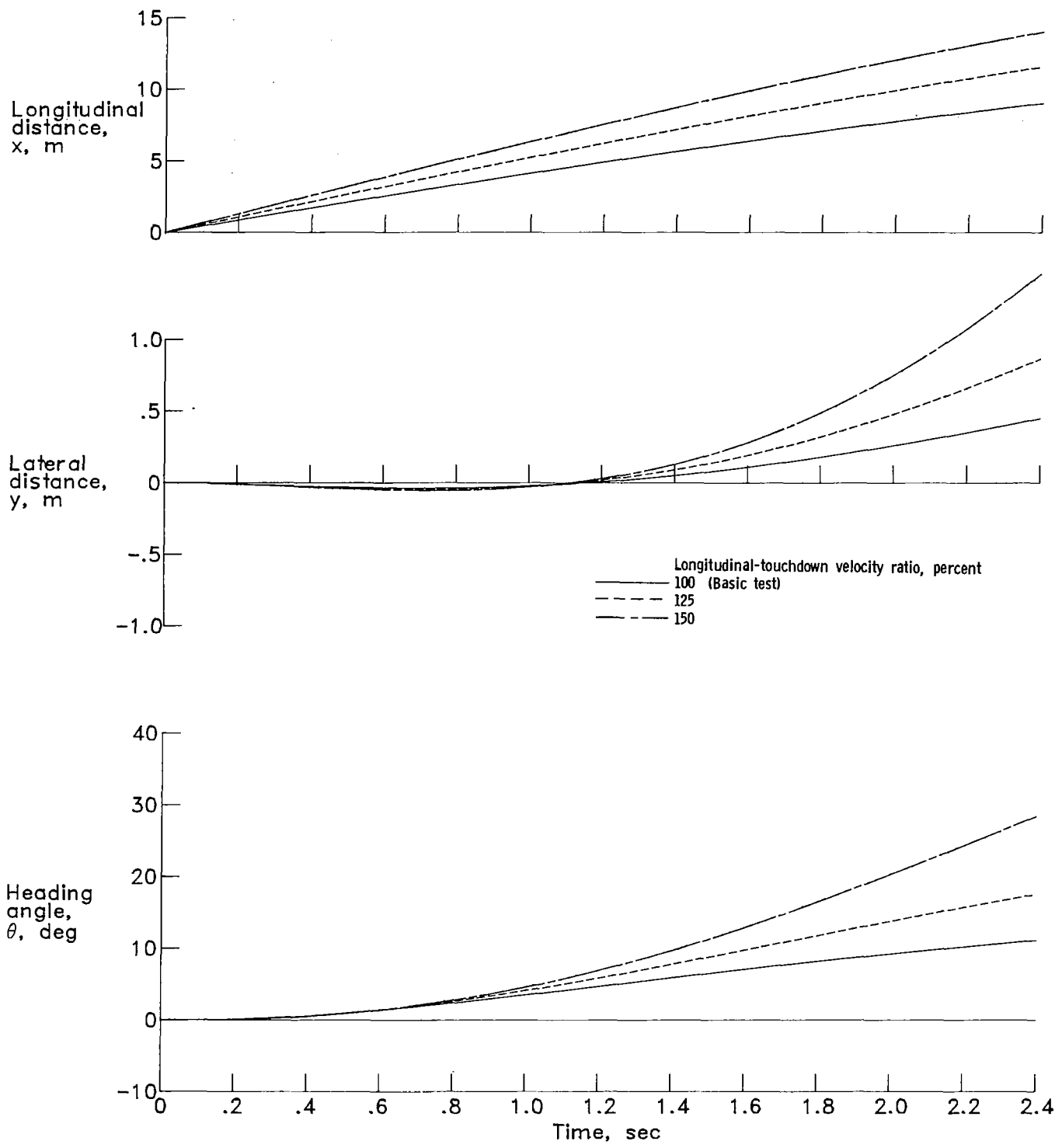


Figure 19.- Computed trajectory-variable time histories of basic-vehicle test with increased longitudinal touchdown velocities.

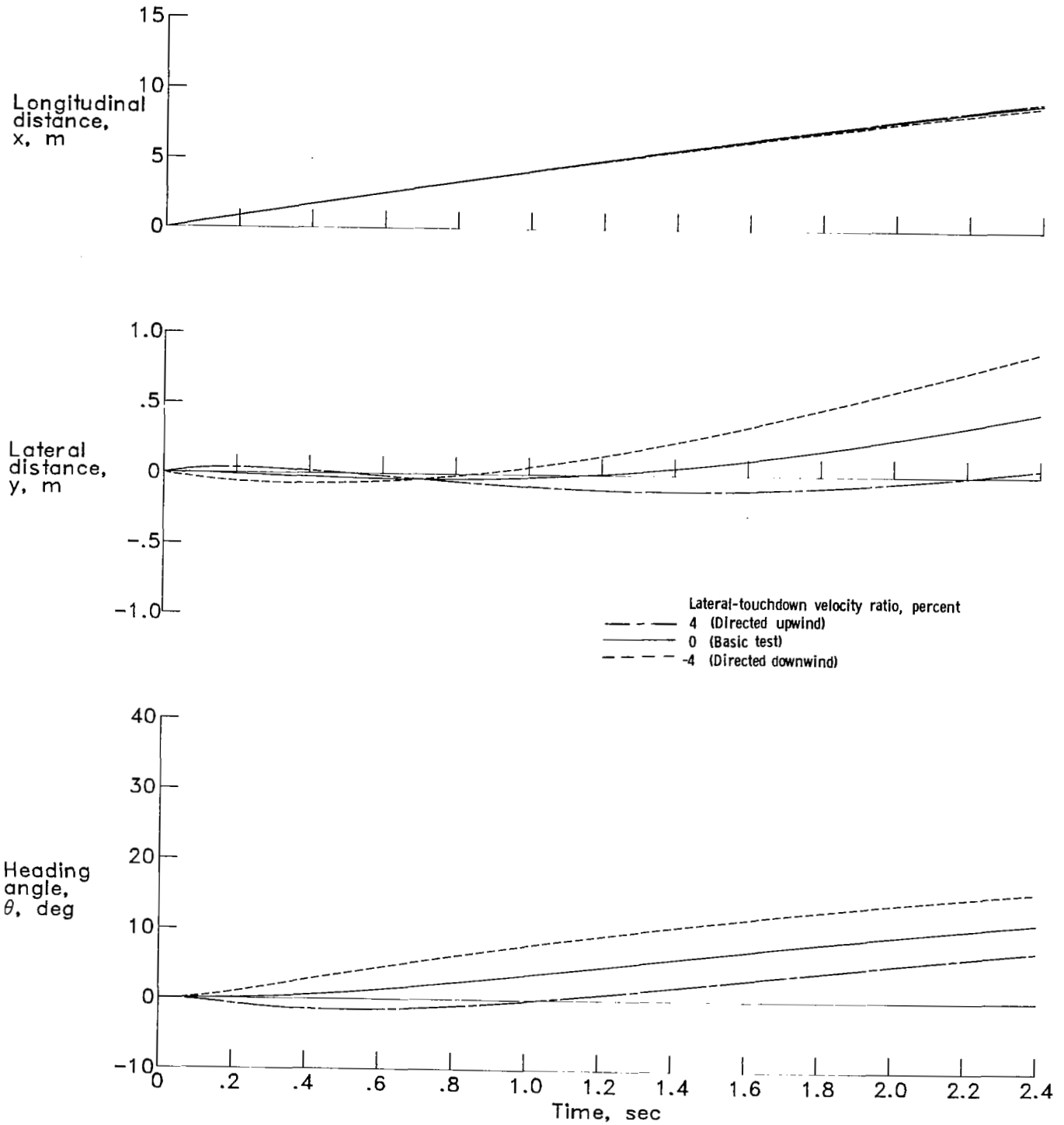


Figure 20.- Computed trajectory-variable time histories of basic-vehicle test with varied lateral touchdown velocities. Velocity ratio refers to basic-test longitudinal velocity.

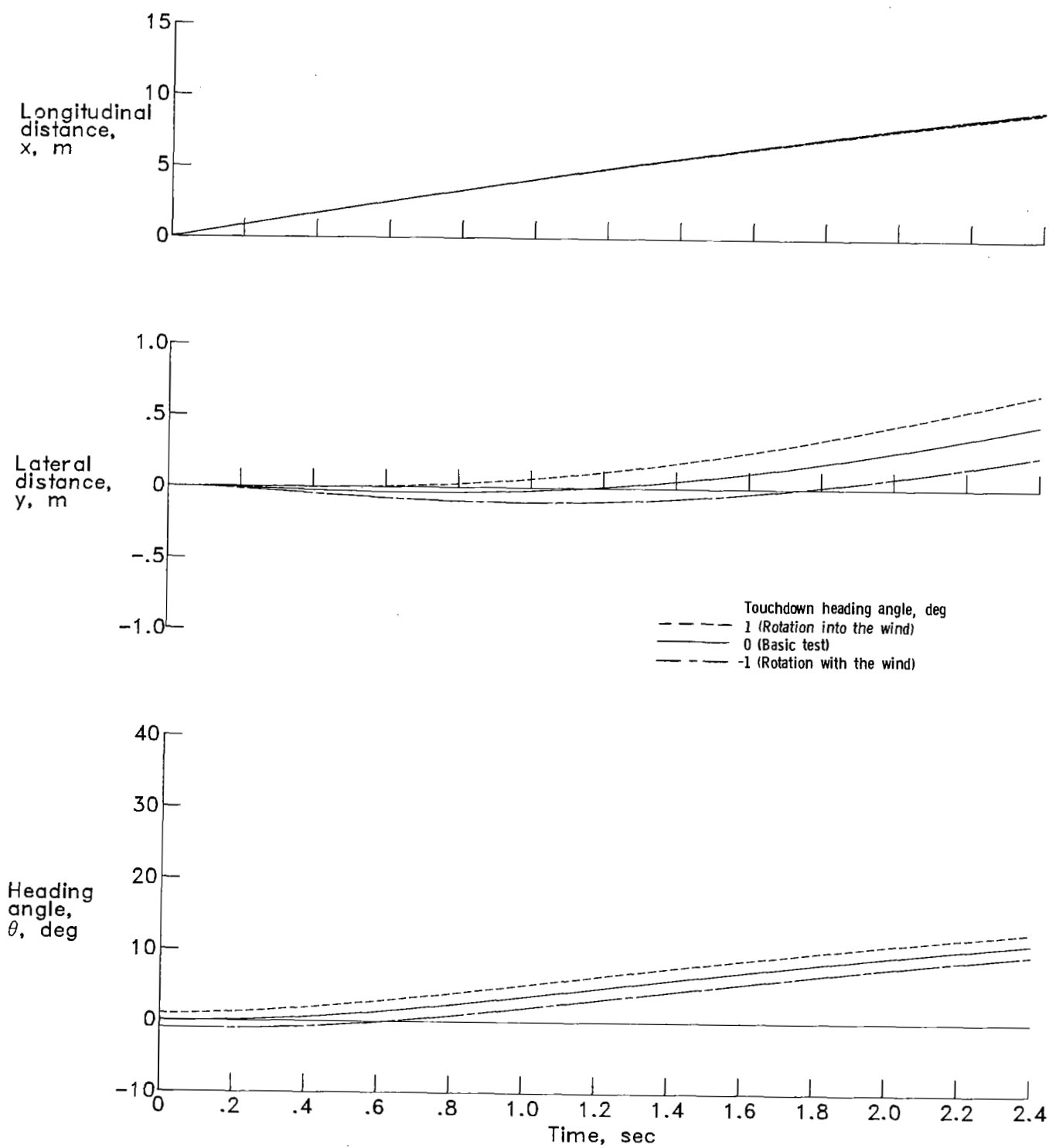


Figure 21.- Computed trajectory-variable time histories of basic-vehicle test with varied touchdown heading angles.

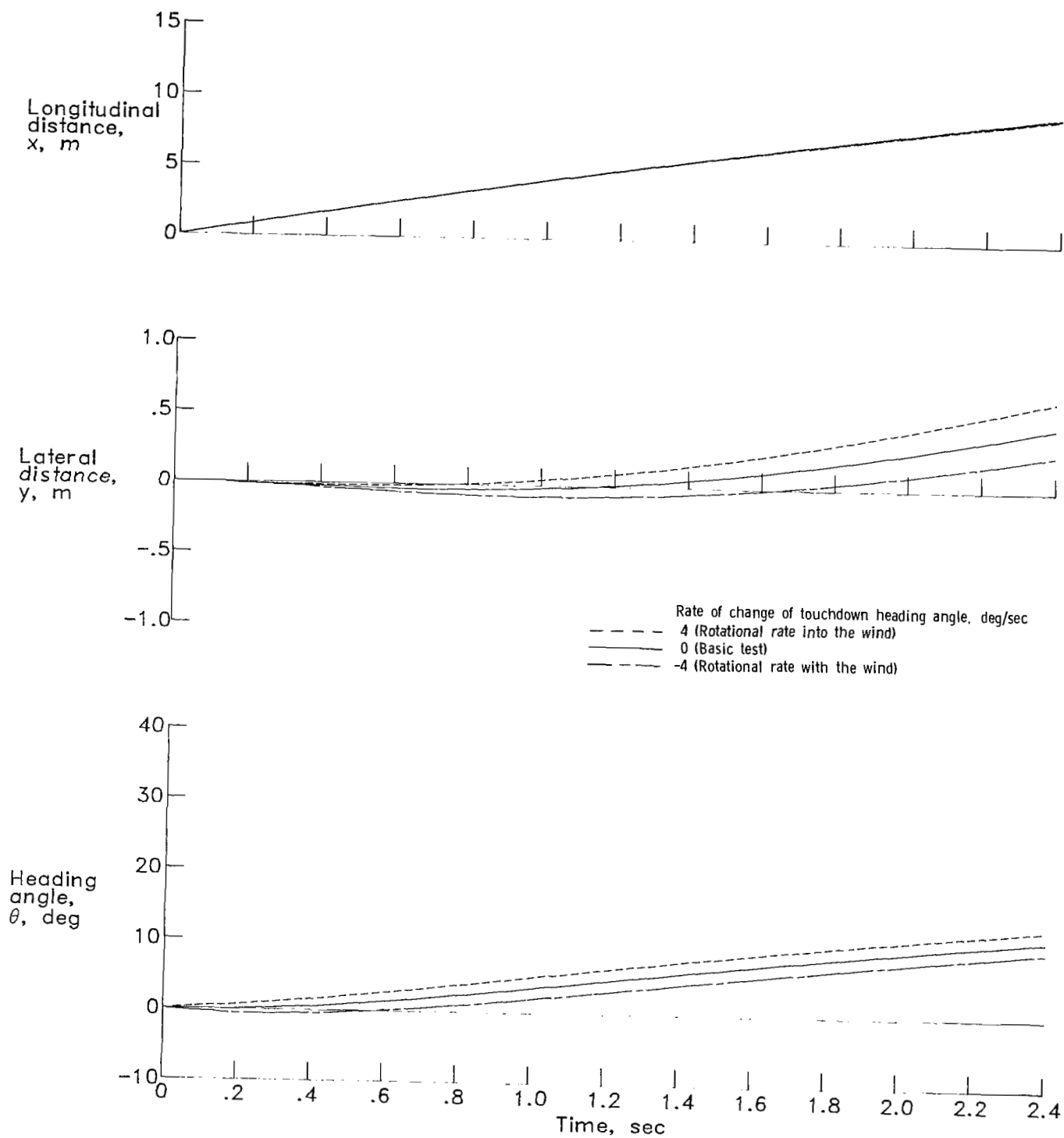


Figure 22.- Computed trajectory-variable time histories of basic-vehicle test with varied rates of change of touchdown heading.

1. Report No. NASA TP-1984		2. Government Accession No.		3. Recipient's Catalog No.	
4. Title and Subtitle PLANAR EQUATIONS OF ROLLOUT MOTION FOR AN AIRCRAFT WITH FREE OR STEERABLE LANDING GEARS				5. Report Date May 1982	
				6. Performing Organization Code 505-44-33-01	
7. Author(s) Robert K. Sleeper and Eunice G. Smith				8. Performing Organization Report No. L-11689	
9. Performing Organization Name and Address NASA Langley Research Center Hampton, VA 23665				10. Work Unit No.	
				11. Contract or Grant No.	
				13. Type of Report and Period Covered Technical Paper	
12. Sponsoring Agency Name and Address National Aeronautics and Space Administration Washington, DC 20546				14. Sponsoring Agency Code	
15. Supplementary Notes					
16. Abstract Equations are derived to predict the rollout behavior of an aircraft in a three-point attitude with freely castoring or steerable landing gears. Transient tire forces are simulated by delaying the application of forces derived from steady-state considerations. Predicted rollout trajectories were similar to those measured in tests of a small-scale landing-gear model equipped with pneumatic tires (where a laterally sloping runway was used to simulate a crosswind), both with and without nose-wheel steering.					
17. Key Words (Suggested by Author(s)) Crosswind landing gears Pneumatic tires Equations of rollout motion			18. Distribution Statement Unclassified - Unlimited Subject Category 05		
19. Security Classif. (of this report) Unclassified		20. Security Classif. (of this page) Unclassified		21. No. of Pages 52	22. Price A04

National Aeronautics and
Space Administration

Washington, D.C.
20546

Official Business
Penalty for Private Use, \$300

THIRD-CLASS BULK RATE

Postage and Fees Paid
National Aeronautics and
Space Administration
NASA-451



2 1 10, A, 042882 500903DS
DEPT OF THE AIR FORCE
AF WEAPONS LABORATORY
ATTN: TECHNICAL LIBRARY (SUL)
KIRTLAND AFB NM 87117

NASA

POSTMASTER:

If Undeliverable (Section 158
Postal Manual) Do Not Return